Research paper

Extreme load analysis of flexible wave energy converters utilising nonlocal continuum damage mechanics

Deepak George[1], Ieuan Collins[1], Ian Masters, Mokarram Hossain *

Zienkiewicz Institute for Modelling, Data and AI, Faculty of Science and Engineering, Swansea University, SA1 8EN, Swansea, United Kingdom

ARTICLE INFO

ABSTRACT

In recent years, there has been a notable increase in interest towards Flexible Wave Energy Converters (FlexWECs). These flexible energy harvesters solve structural design challenges faced by rigid-body WECs by responding to external loading by changing shapes. Typically, the structures are made from rubber-like materials which pose few challenges from a material modelling point of view. Firstly, the material is in the finite strain regime requiring a hyperelastic modelling approach, but more critically the material response is expected to change during the operational lifetime. There is softening from both time-dependent viscoelasticity and micro-void growth caused by fatigue loading. The goal of this paper is to understand the latter mechanism and how it manifests within a membrane. To account for this damage accumulation, the gradient-enhanced nonlocal damage model is coupled to a hyperelastic Neo-Hookean constitutive law. The framework has been implemented in the commercial finite element software ABAQUS by exploiting its fully coupled thermo-mechanical formulation. A parametric study is performed on two FlexWEC archetypes: a submerged pressure differential and a floating bulge wave attenuator. The performance evaluation of these devices is carried out by analysing the evolution of the pressure–volume relation and pressure-stretch relation, respectively. The results show that the nonlocal aspects of damage in the pressure differential FlexWECs are small due to membrane action, but the saturation of damage does affect the pressure–volume function of each membrane. However, in the case of attenuator, the damage regularisation plays a crucial role in its behaviour due to the steep stress gradient from the crest of the wave. The outcomes from these analyses suggest FlexWEC design is advantageous from a fatigue loading perspective as it always reaches an equilibrium state which minimises the stress-differential, reducing the likelihood of localised crack growth.

1. Introduction

Since the latter half of the 20th century, ocean wave energy has been actively investigated as a promising renewable energy resource. Owing to its abundance and high energy density (Clément et al., 2002), wave energy presents a huge opportunity to help countries meet their net-zero targets. Conventional wave energy converter designs have captured this energy using a rigid body hydrodynamic interface, e.g., floater, buoy, pitching flap etc. The kinetic energy of this interface is converted to electrical energy at a Power Take-Off (PTO) (Yemm et al., 2012; LLC, 2022) . However, there has been a lack of breakthrough designs achieving commercialisation, contrary to other renewable energy technologies. This is partly due to the significant engineering challenges from corrosive mechanisms and highly variable loading cycles; a stormy sea state can be an order of magnitude

greater than a calm one. To withstand these harsh conditions, wave energy devices consist of large heavy metallic machinery with a high capital expenditure and low operational bandwidth. To address these issues, wave energy developers, academics and governmental bodies have made a paradigm shift to more compliant structures, with the aim of improving reliability, efficiency and cost. Even within flexible structure designs, there is a hierarchy of integration. Flexible Wave Energy Converter (FlexWEC) patents date back to the 1970s (French, 1979), with renewed interest in 2010s (Farley and Rainey, 2011). These designs replace the rigid body primary mover with a membrane-like structure which can adapt to external loading through changing shape. However, they still keep rigid elements such as the PTO and housing structure (Babarit, 2018; Pecher and Kofoed, 2017; Milani et al., 2023; Renzi et al., 2021; Abad et al., 2023).

Direct Generation (DG) (Anon, 2023d) and Distributed Energy Converter Technologies (DEEC-Tec) (Anon, 2023b) fully integrate the energy generation into the compliant structure, leading to potentially even greater cost savings. This can be achieved using Dielectric Elastomer Generators (DEGs) (Moretti et al., 2020b; Koh et al., 2010) and Dielectric Fluid Generators (DFGs) (Duranti et al., 2017) which harvest energy through the principle of varying capacitance. The two funded design competitions by Wave Energy Scotland (WES) (Anon, 2023a) and the US Department of Energy (Anon, 2023c) aim to provide the first steps in concept design generation of these technologies. For a review of the state-of-the-art FlexWEC and Direct Generation technologies, see Collins et al. (2021) and Moretti et al. (2020a).

One crucial consideration when designing these WECs revolves around the selection of the appropriate material. FlexWECs can experience strains of up to 100%, while DG WECs may go beyond 200% due to the necessity of varying capacitance. Additionally, for an economically viable design, these structures must endure a substantial number of cycles, ranging from 10^6 to 10^7 cycles. To meet these demanding requirements, elastomeric composites emerge as a promising choice due to their exceptional stretchability and well-documented fatigue resistance [REF]. However, working with elastomers introduces its own set of challenges, including changes in mechanical properties due to viscoelasticity and fatigue. Collins et al. (2023) have demonstrated that viscoelasticity can lead to issues such as creep and alterations in the pressurisation properties of pneumatic FlexWECs. It is worth noting that the levels of hysteresis remained relatively low when strains were below 100%. On the other hand, fatigue damage results in a gradual softening of the material over tens of thousands of cycles, which has the potential to adversely affect the performance of the device, i.e. lower operational bandwidth from a reduced pressurisation window (Esmaeili et al., 2023). Furthermore, it is important to consider that this softening process may be further exacerbated by other sources of damage, such as chemical ageing and biofouling caused by the marine environment. Consequently, gaining a comprehensive understanding of the device's performance throughout the entire material life cycle becomes crucial, as it allows to make accurate predictions regarding the decay in power output over time. This understanding is not only critical for forecasting performance degradation but also for minimising the risk of catastrophic failures resulting from the development of significant cracks in the material and structural instabilities.

From a numerical perspective, computational mechanics models represent a vital tool for validating different design configurations. In quasi-brittle materials, the formation of macro-cracks through the concentration of micro-cracks is modelled using Continuum Damage Mechanics (CDM) with two main approaches. The first approach is based on the local action of stress concentration and the development of cracks (Holzapfel, 2000). One of the earliest studies in this field was due to Kachanov (1958) wherein a reduction in the stress-bearing area is considered to model creep failure. A detailed review of local methods can be found in Krajcinovic and Lemaitre (1987) and Lemaitre and Chaboche (1990). One of the main disadvantages of these local methods is that they fail to give meaningful results due to the loss of ellipticity. Hence the mathematical system becomes ill-posed and fails to converge. This is also apparent from the mesh-dependent nature of the damage zone. On top of that such a theory assumes that the material is homogeneous at every length scale, however in reality, there exists a length scale below which the material is heterogeneous. Hence, the nonlocal distribution of damage becomes necessary. The second approach is generally referred to as the nonlocal damage model which ensures the nonlocality by introducing an internal length scale parameter which regularises the damage. This can further be accomplished by two approaches namely integral-type and gradient type. For instance, Bažant and Jirásek (2002) and Bažant and Pijaudier-Cabot (1988) used an integral-based formulation in which the spatially weighted averages of the internal variable is introduced as a nonlocal variable for the damage regularisation. However, these come with

complications related to linearisation and add to the computational effort (Waffenschmidt et al., 2014). On the other hand, the gradient-based approach introduces higher-order gradient terms of the nonlocal variables, see Lasry and Belytschko (1988), Mühlhaus and Alfantis (1991), Polizzotto et al. (1998), Eringen and Wegner (2003), Umesh and Rajagopal (2019), Rawat et al. (2021). This results in an additional Euler–Lagrange equation and its boundary condition in the nonlocal variable. Readers are directed to some of the pioneering works on gradient-based damage models by Pamin (1994), de Borst and Pamin (1996), Peerlings et al. (1996a,b), Dimitrijevic and Hackl (2007), Liebe et al. (2001), Steinmann (1999). Recently Waffenschmidt et al. (2014) provided a detailed algorithmic implementation of a nonlocal gradient-enhanced continuum damage model at finite strains.

Phase-field modelling is another class of nonlocal damage models which concentrate on a finite zone with steep gradients in the vicinity of discontinuity due to cracks. de Borst and Verhoosel (2016) provides a detailed comparison between gradient-enhanced and phase-field nonlocal damage models. Despite the numerous advantages of the phase-field models (Denli et al., 2020; Konica and Sain, 2023; Dal et al., 2022), a gradient-enhanced model is of more interest due to its ease of implementation in a commercial software such as through the interface of the user subroutine (UMAT) format of ABAQUS, whereas a phase-field nonlocal model requires the implementation at an element formulation level. This was shown by Ostwald et al. (2019), where the similarity of the gradient-based damage model with the steady-state temperature equation is explored to use a coupled temperature–displacement element (already devised in ABAQUS) to simulate the evolution of damage. The finite strain formulations followed the same derivation process as performed by Waffenschmidt et al. (2014).

Modelling damage is not the full story since the geometry of the WEC needs to be accurately discretised and modelled under the appropriate boundary conditions. For WECs, it is necessary to perform a fluid–structure interaction (FSI) analysis. Although using membrane-like structures presents a significant numerical challenge, due to the strong inertial effects of the fluid acting on the membrane. As a result, previous studies have simplified the model using analytical representations for membrane mechanics, see earlier work by Selby and Shannon (2009). Some studies have tried to couple CFD with FEM, although the computational cost remains too significant for widely accepted use.

In this work, there were two main goals: firstly to understand how damage affects the device under different loading conditions. Secondly, to understand the effect of nonlocality of the damage accumulation and the resulting failure mode shape. To achieve these goals, as a first step we adopted the already devised methodology presented by Ostwald et al. (2019) for finite element simulations. The finite strain hyperelasticity model is coupled with gradient enhanced nonlocal damage model to predict the onset and the propagation of damage. The FlexWEC style devices and strain duty (<100%) were chosen to keep consistent with the previous work of Collins et al. (2023). Since the damage mechanisms are the primary focus of this work, the FSI problem is simplified to only consider the performance of the membrane structure to the changing external fluid pressure. This is achieved by decoupling the external force from the membrane deformation and is assumed to be a function of the wave height thereby resulting in a quasi-static condition. Numerous literature can be found that use such methodology to simplify the analysis (Selby and Shannon, 2009; Eriksson et al., 2016; Bonet et al., 2000; Verron et al., 2001; Coelho et al., 2014).

This paper is organised into the following sections: Section 2 provides a detailed overview of a gradient-enhanced damage model. Here we talk about the kinematics of the problem, strain energy enhancement, key governing equations leading to the coupled boundary value problem. Further, this section also explains the ABAQUS implementation using the UMAT format and damage evolution, irreversibility condition leading to the update of the history variable using a Newton–Raphson scheme. In Section 3, numerical validation of our ABAQUS implementation is demonstrated through two examples available in the

literature. Section 4 deals with the numerical examples and parametric study of two classical FlexWECs namely a stadium geometry and a tube geometry. This is followed by a detailed discussion on the effects of damage mechanisms on the performance of each device. Further, the study is concluded with a brief summary and conclusions in Section 5.

2. Numerical implementation of a gradient-enhanced nonlocal damage model

This section gives an elaborate description of the algorithmic forms of a gradient-enhanced nonlocal damage model and its ABAQUS implementation. Noteworthy to mention here that ABAQUS or any other user-friendly commercial software does not have any nonlocal damage models implemented as a standard scheme. Hence, the UMAT subroutine interface of ABAQUS enabling a user to implement any custom constitutive models is adopted here. Fig. 1 illustrates the solution procedure in ABAQUS UMAT originally designed for a thermo-mechanically coupled problem which is exploited here as it has algorithmic similarities with a gradient-enhanced nonlocal damage model. The input file contains all the information about the model such as geometry, mesh, material parameters, and boundary conditions. The file is submitted for analysis using ABAQUS COMMAND in conjunction with the UMAT.for file (in FORTRAN format). For the efficient calculation of results, the UMAT subroutine requires the calculation of six parameters as described in Table 1 for a coupled temperature–displacement problem (same as in the case of nonlocal damage model). Once the solution process is finished, ABAQUS CAE is used to view the results stored in the $*$.odb file. Furthermore, suitable Python and Matlab scripts can be used to generate the figures presented in this work.

The first and foremost step in solving a continuum problem at finite strain is establishing its kinematics. The deformation of a body can be mathematically expressed in terms of a mapping φ which relates its final coordinates to the initial coordinates. Let $\mathbf{x} = \varphi(\mathbf{X}, t)$ denotes the deformation map of a body represented by $\mathcal{B}_0 \subset \mathbb{R}^3$ at the reference configuration and $\mathcal{B} \subset \mathbb{R}^3$ at the current configuration where $\mathbf{X}$ denotes the reference configuration such that $\mathbf{X} \in \mathcal{B}_0$ and $\mathbf{x} \in \mathcal{B}$ represents the spatial configuration. The two-point deformation gradient tensor $\mathbf{F}$ is defined by the referential gradient of the deformation map as

$$\mathbf{F} = \frac{\partial \varphi}{\partial \mathbf{X}} = \nabla_0 \varphi \qquad (1)$$

and $J = \det \mathbf{F}$ is the Jacobian of the deformation gradient $\mathbf{F}$. In order to account for the nearly-incompressible behaviour of rubber-like materials, the deformation gradient is usually decomposed into a volumetric part and an isochoric part, i.e., $\mathbf{F} = \mathbf{F}_{vol} \mathbf{F}_{iso} = \mathbf{F}_{vol} \bar{\mathbf{F}}$, where $\mathbf{F}_{vol} = J^{\frac{1}{3}} \mathbf{I}$, $\mathbf{I}_{ij} = \delta_{ij}$. This classical decomposition usually used for rubber-like materials results in a volumetric–isochoric decomposition of the total energy function, i.e. $\Psi_{int} = \Psi_{vol}(J) + \Psi_{iso}(\bar{\mathbf{F}})$. The damage regularisation is achieved by adding the nonlocal contribution of damage progression to the standard strain energy density function. Thus the enhanced energy density reads as:

$$\Psi_{int}(\mathbf{F}, \phi, \nabla_0\phi, k) = \Psi_{loc}^{vol}(J) + f(k)\Psi_{loc}^{iso}(\bar{\mathbf{F}}) + \Psi_{nloc}^{grad}(\mathbf{F}, \nabla_0\phi) + \Psi_{nloc}^{plty}(\phi, k) \quad (2)$$

Here, k is the history variable and ϕ is the nonlocal damage variable. In Eq. (2), $f(k)$ denotes the damage function which degrades only the isochoric part of the energy density ($\Psi_{loc}^{iso}(\mathbf{F})$) such that

$$f(k) : \mathbb{R}^+ \to (0, 1] \mid \left\{ f(0) = 1, \lim_{k \to +\infty} f(k) \to 0 \right\} \qquad (3)$$

As standard, the local contribution is decomposed into volumetric and isochoric components such that $\Psi_{loc}^{vol}(J) = \frac{K}{2}[J-1]^2$ and $\Psi_{loc}^{iso}(\bar{\mathbf{F}}) = \frac{\mu}{2}[\bar{I}_1 - 3]$, where $\bar{I}_1 = \text{tr}(\bar{\mathbf{F}}^T \cdot \bar{\mathbf{F}})$ and K is the bulk modulus, μ is the shear modulus. Note that, for simplicity, we take simple forms of volumetric and isochoric parts of the energy function. For more advanced volumetric and isochoric energy functions, see Hossain and Steinmann (2013), Steinmann et al. (2012). Further, the nonlocal contribution is
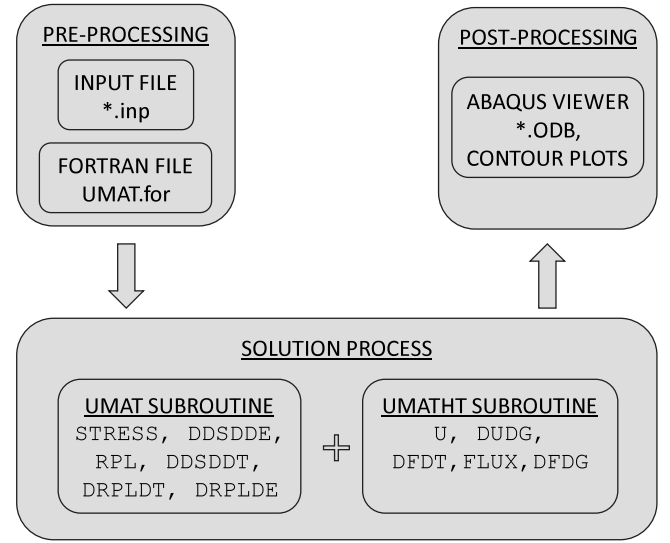

Fig. 1. Flowchart illustrating the solution strategy of ABAQUS and variable definitions using user subroutines UMAT and UMATHT.

Table 1
Overview of the variables that need to be defined in the UMAT subroutine for a coupled temperature–displacement problem.

UMAT variable	Definition
STRESS	Cauchy's stress
DDSDDE	Jacobian matrix
DDSDDT	Variation of stress increments with respect to temperature
RPL	Volumetric heat generation
DRPLDE	Variation of stress with respect to strain increments
DRPLDT	Variation of RPL with respect to temperature

added in two steps as $\Psi_{nloc}^{grad} = \frac{c_d}{2} \nabla_0\phi \cdot \mathbf{C}^{-1} \cdot \nabla_0\phi = \frac{c_d}{2} \nabla\phi \cdot \nabla\phi$ and $\Psi_{nloc}^{plty} = \frac{\beta_d}{2}[\phi - k]^2$ such that Ψ_{nloc}^{grad} introduces the gradient of ϕ and Ψ_{nloc}^{plty} adds a penalty for the difference between ϕ and k. Therein, c_d is the damage regularisation parameter β_d is the penalty parameter and the material and spatial gradients are related by $\nabla_0\phi = \nabla\phi \cdot \mathbf{F}$ where $\nabla = \frac{\partial}{\partial \mathbf{x}}$. The present work assumes a hyperelastic behaviour of the membrane material and adopts the classical nearly incompressible Neo-Hookean model for the strain energy density function for simplicity. However, other advanced strain energy functions suitable for hyperelastic materials are straightforward to apply. Further incorporating the definitions of Ψ_{nloc}^{grad} and Ψ_{nloc}^{plty}, the internal contribution of the strain energy density becomes

$$\Psi_{int}(\mathbf{F}, \phi, \nabla_0\phi, k) = \frac{K}{2}[J-1]^2 + f(k)\frac{\mu}{2}[\bar{I}_1 - 3]$$
$$+ \frac{c_d}{2} \nabla_0\phi \cdot \mathbf{C}^{-1} \cdot \nabla_0\phi + \frac{\beta_d}{2}[\phi - k]^2 \qquad (4)$$

The present study assumes that the damage in rubber-like materials is concentrated on the isochoric part of the strain energy density function, see Jha et al. (2019). A common choice of $f(k)$ is adopted satisfying equation Eq. (3)

$$f(k) := e^{(-\eta_d[k - k_d])} \qquad (5)$$

where η_d is the damage saturation parameter and k_d is the damage initiation parameter. Now the total potential energy of the system is obtained by integrating the total strain energy density function over the entire domain, e.g.,

$$\Pi_{tot} = \Pi_{int} + \Pi_{ext} \qquad (6)$$
$$= \int_{\mathcal{B}_0} \Psi_{int} + \int_{\mathcal{B}_0} \Psi_{ext}^{vol} + \int_{\partial\mathcal{B}_0} \Psi_{ext}^{sur} \qquad (7)$$

where $\Psi_{\text{ext}}^{\text{vol}}$ and $\Psi_{\text{ext}}^{\text{sur}}$ represent the body force per unit volume and the traction force per unit area in the reference configuration, respectively. By invoking the principle of minimum potential energy and applying the product rule and Gauss' divergence theorem, the strong forms in reference configuration are obtained as

$$\boldsymbol{\nabla}_0 \cdot \mathbf{P} + \mathbf{B} = \mathbf{0} \quad \text{in} \quad \mathcal{B}_0 \tag{8}$$

$$\mathbf{P} \cdot \mathbf{N} = \mathbf{T} \quad \text{on} \quad \partial\mathcal{B}_0 \tag{9}$$

$$\boldsymbol{\nabla}_0 \cdot \mathbf{Y} + Y = 0 \quad \text{in} \quad \mathcal{B}_0 \tag{10}$$

$$\mathbf{Y} \cdot \mathbf{N} = 0 \quad \text{on} \quad \mathcal{B} \tag{11}$$

where, the first Piola stress $\mathbf{P} = \partial_{\mathbf{F}}\Psi_{\text{int}}$ and $\mathbf{Y} = \partial_{\boldsymbol{\nabla}_0\phi}\Psi_{\text{int}}$ are flux terms and $Y = -\partial_\phi\Psi$ and $\mathbf{B}$ are source terms. The corresponding strong forms in the spatial configuration are obtained by performing the transformations on flux-like quantities as $\mathbf{y} = J^{-1}\mathbf{Y}\mathbf{F}^T$ and source terms as $\mathbf{b} = J^{-1}\mathbf{B}$, leading to

$$\boldsymbol{\nabla} \cdot \boldsymbol{\sigma} + \mathbf{b} = \mathbf{0} \quad \text{in} \quad \mathcal{B} \tag{12}$$

$$\boldsymbol{\sigma} \cdot \mathbf{n} = \mathbf{t} \quad \text{on} \quad \mathcal{B}^\sigma \tag{13}$$

$$-c_d \boldsymbol{\nabla} \cdot [\boldsymbol{\nabla}\phi] = \beta_d[k - \phi] \quad \text{in} \quad \mathcal{B} \tag{14}$$

$$\boldsymbol{\nabla}\phi \cdot \mathbf{n} = 0 \quad \text{on} \quad \mathcal{B} \tag{15}$$

Here, the damage variable (ϕ) satisfies the zero flux condition in the whole boundary resulting in the so-called natural boundary condition. Following the standard definition, the second Piola–Kirchhoff's stress is expressed as (Hossain and Steinmann, 2013; Steinmann et al., 2012)

$$\mathbf{S} = \mathbf{S}_{\text{vol}} + \mathbf{S}_{\text{iso}}, \tag{16}$$

$$\mathbf{S} = 2\frac{\partial\Psi_{\text{int}}}{\partial\mathbf{C}} = KJ\,[J-1]\,\mathbf{I} + f(k)\mu J^{-2/3}\Big[\mathbb{I} - \frac{1}{3}\mathbf{C}^{-1}\otimes\mathbf{C}\Big] : \mathbf{I} \tag{17}$$

where, $\mathbb{I}_{ijkl} = \delta_{ik}\delta_{jl}$ and $\mathbf{I}_{ij} = \delta_{ij}$. Since ABAQUS requires the evaluation of Cauchy stress $\boldsymbol{\sigma}$, the push-forward operation is employed and the result is stored in a Voigt notation in the variable STRESS,

$$\boldsymbol{\sigma} = J^{-1}\mathbf{F} \cdot \mathbf{S} \cdot \mathbf{F}. \tag{18}$$

Similarly, the tangent matrix is also defined as follows:

$$\mathbb{d}_{ijkl} = \frac{1}{J}\left[F_{iI}F_{jJ}F_{kK}F_{lL}C_{IJKL} + \frac{1}{2}\left[\delta_{ik}\sigma_{jl} + \delta_{jl}\sigma_{ik} + \delta_{il}\sigma_{jk} + \delta_{jk}\sigma_{il}\right]\right] \tag{19}$$

where

$$C_{IJKL} = 2\frac{\partial S_{IJ}}{C_{KL}} \tag{20}$$

The tangent matrix $\mathbb{d}$ thus calculated is stored in a Voigt (matrix–vector) notation in the variable DDSDDE of ABAQUS. The necessary ingredients required for the UMAT implementation of a hyperelastic problem is complete now. However, the computation of the fully coupled tangent matrix requires the calculation of some additional variables. The variation of the stress with respect to the damage variable is defined as

$$\frac{\mathrm{d}\boldsymbol{\sigma}}{\mathrm{d}\phi} = \mathbf{F} \cdot \frac{\mathrm{d}\mathbf{S}}{\mathrm{d}\phi} \cdot \mathbf{F}^T \tag{21}$$

which is stored in the variable DDSDDT. Now the damage component of the algorithm needs to be defined. Firstly the damage source term is stored in the variable RPL following Eq. (14) as

$$r_\theta = r_\phi = \text{RPL} = \beta_d[k - \phi] \tag{22}$$

Please note that in the current implementation damage variable ϕ and temperature variable (θ) are analogous. Further the sensitivities of RPL with respect to the damage variable and strain need to be defined where,

$$\text{DRPLDT} = \frac{\mathrm{d}(\text{RPL})}{\mathrm{d}\phi} = \beta_d\left[\frac{\mathrm{d}k}{\mathrm{d}\phi} - 1\right] \tag{23}$$

$$\text{DRPLDE} = \mathbf{F} \cdot \frac{\mathrm{d}(\text{RPL})}{\mathrm{d}\mathbf{C}} \cdot \mathbf{F}^T = \beta_d\mathbf{F} \cdot \frac{\mathrm{d}k}{\mathrm{d}\mathbf{C}} \cdot \mathbf{F}^T \tag{24}$$

The current UMAT is implemented in the set of reference configuration. Hence, the push forward operation is required to obtain the corresponding values of relevant quantities (e.g., stress in Eq. (16) and tangent operator in Eq. (20)) in the current configuration.

2.1. Weak forms and linearisation

The coupled system of equations is solved in the finite element framework by establishing the weak forms and the corresponding residuals as follows

$$\mathbf{r}_u = \int_\mathcal{B} \boldsymbol{\sigma} : \boldsymbol{\nabla}\mathbf{w}^u \mathrm{d}\upsilon - \int_\mathcal{B} \mathbf{b} \cdot \mathbf{w}^u \mathrm{d}\upsilon - \int_{\Gamma_n} \mathbf{t} \cdot \mathbf{w}^u \mathrm{d}a = \mathbf{0}, \forall \mathbf{w}^u \in \mathcal{W}_\mathbf{u} \tag{25}$$

$$\mathbf{r}_\phi = \int_\mathcal{B} \boldsymbol{\nabla}\phi \cdot \boldsymbol{\nabla}w^\phi \mathrm{d}\upsilon - \int_\mathcal{B} \beta_d(k-\phi)w^\phi \mathrm{d}\upsilon = 0, \forall w^\phi \in \mathcal{W}_\phi \tag{26}$$

where, $\mathcal{W}_\mathbf{u}$ and $\mathcal{W}_\phi$ are the test function spaces for the displacement field $\mathbf{u}$ and nonlocal damage field ϕ, respectively. Further, the linearised system of equations of the coupled problem can be represented on an element level as

$$\begin{bmatrix} \mathbf{K}_{uu}^e & \mathbf{K}_{u\phi}^e \\ \mathbf{K}_{\phi u}^e & \mathbf{K}_{\phi\phi}^e \end{bmatrix} \begin{bmatrix} \Delta\mathbf{u}^e \\ \Delta\phi^e \end{bmatrix} = \begin{bmatrix} \mathbf{r}_u^e \\ \mathbf{r}_\phi^e \end{bmatrix} \tag{27}$$

where,

$$\mathbf{K}_{uu}^e = \frac{\mathrm{d}\mathbf{r}_u^e}{\mathrm{d}\mathbf{u}}; \quad \mathbf{K}_{u\phi}^e = \frac{\mathrm{d}\mathbf{r}_u^e}{\mathrm{d}\phi}; \quad \mathbf{K}_{\phi u}^e = \frac{\mathrm{d}\mathbf{r}_\phi^e}{\mathrm{d}\mathbf{u}}; \quad \mathbf{K}_{\phi\phi}^e = \frac{\mathrm{d}\mathbf{r}_\phi^e}{\mathrm{d}\phi}$$

It is important to note that the weak forms and the subsequent linearisation presented here illustrate the coupled system for a compressible material. However, when the material response approaches incompressibility, the displacement formulation often cannot yield meaningful results. Due to the high ratio of bulk to shear modulus, the stiffness matrix becomes singular for nearly incompressible problems. Moreover, the stress values can exhibit large oscillations at integration points within an element, unless a reduced integration is used. Numerous techniques like mixed formulation, three-field formulation, selective reduced integration with hourglass control, enhanced-strain method, $\bar{\mathbf{F}}$ method etc. exist in the literature to overcome this problem (Kadapa and Hossain, 2022; Kadapa et al., 2016; Kadapa, 2019; de Souza Neto et al., 1996; Neto et al., 2005). ABAQUS uses a mixed formulation in which a new variable to represent the volume change $\hat{J}$ is introduced (Anon, 2021). Further, the strain energy density is augmented by introducing the constraint $J - \hat{J} = 0$ with the help of a Lagrangian multiplier $\hat{p} = -\frac{\partial U(\hat{J})}{\partial\hat{J}}$. The formulation can be accessed by using hybrid elements in conjunction with the total formulation in ABAQUS UMAT. $\hat{J}$ is made available in UMAT at STRESS(NTENS+1) as a read only variable where NTENS is the number of independent stress variables. Further, the following additional derivatives need to be supplied in UMAT: $\hat{K} = \frac{\partial^2 U}{\partial\hat{J}^2}$ and $\frac{\partial\hat{K}}{\partial\hat{J}}$ at STRESS(NTENS+2) and STRESS(NTENS+3) respectively. Thus a nearly incompressible problem can be solved effectively in ABAQUS using hybrid elements.

2.2. Damage evolution and irreversibility

The previous section fully defines the coupled system whereby the sensitivities of the stress and the damage source with respect to the field variables are defined. However, the damage initiation and its irreversibility condition need to be addressed. In order to understand both conditions, the thermodynamics of the damage process needs to be explored. Following the procedure put forward by Waffenschmidt et al. (2014), the thermodynamic driving force of the damage can be expressed as

$$g = -\frac{\partial\Psi_{\text{int}}}{\partial d} = \Psi_{\text{iso}} + \beta_d\,[\phi - k]\,\frac{\partial k}{\partial d} \tag{28}$$

where, $d = 1 - f(k)$ gives the extend of damage such that

$$d = \begin{cases} 0 & \text{pristine} \\ 1 & \text{fully damaged} \end{cases} \tag{29}$$

(a) 3D block under compression: boundary conditions.

(b) Displacement profile of the 3D block under compression

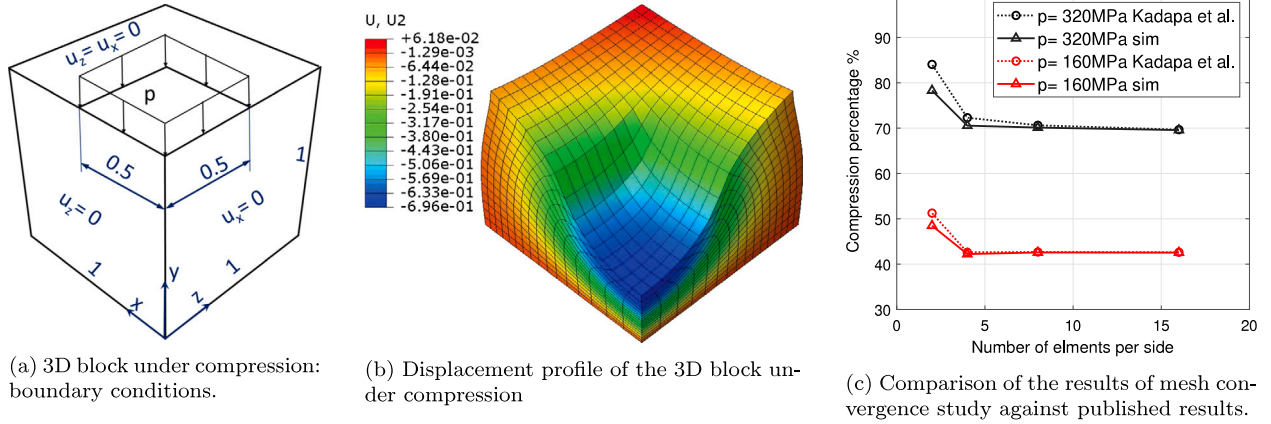(c) Comparison of the results of mesh convergence study against published results.

Fig. 2. A 3D-block under compression: sketch of the problem with boundary conditions, displacement profile and comparison of mesh convergence results with Kadapa and Hossain (2022).
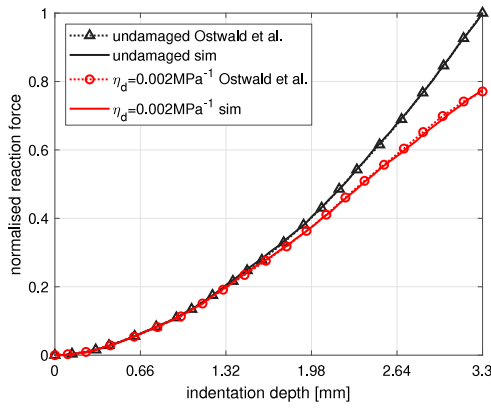

Fig. 3. Comparison of load–displacement curves with that of Ostwald et al. (2019). Black lines represent the undamaged case whereas the red lines represent the damaged case for $\eta_d = 0.002$ MPa^{-1}. Further the dotted lines correspond to Ostwald's results and the firm lines are that of the current simulation results.

Now a damage condition function $\Phi_d \leq 0$ can be defined to describe the state of the material such that

$$\Phi_d \begin{cases} < 0 & \text{elastic} \\ = 0 & \text{damage} \end{cases} \tag{30}$$

Now the damage condition is defined in terms of the history variable as

$$\Phi_d = g - k \leq 0 \tag{31}$$

Further, the damage irreversibility is ensured by the so-called Karush–Kuhn–Tucker condition where,

$$\dot{k} \geq 0, \ \Phi_d \leq 0, \ \dot{k}\Phi_d = 0 \tag{32}$$

Since Eq. (31) is nonlinear in k, the value of k for the current increment is sought in an implicit Backward Euler scheme using the Newton–Raphson method, where the implicit scheme ensures an unconditional stability. Thus the updated k is evaluated as

$$k_{n+1} = k_n + \Delta k_{n+1} \tag{33}$$

where,

$$\Delta k_{n+1}^{p+1} = \Delta k_{n+1}^p - \left[\frac{\mathrm{d}\Phi_d|_{k_{n+1}^p}}{\mathrm{d}\Delta k_{n+1}^p} \right]^{-1} \Phi_d|_{k_{n+1}^p} \tag{34}$$

Here, p denotes the Newton–Raphson iteration and n corresponds to the load step number. Thus the updated history variable k satisfying

Eq. (31) is used to calculate the degradation function $f(k)$ leading to the assessment of the extend of damage d.

3. Validation of the UMAT implementation

In this section, the UMAT implementation of the damage model is validated against other published data. This is done in two steps. Firstly, the competence of the nearly incompressible implementation is validated against the well-known example of 3-D block under compression. This is important because the hybrid elements used in ABAQUS are made effective in nearly incompressible regimes by altering the UMAT to account for the modified variable $\hat{J}$. In the second example, the gradient-enhanced damage model is validated for a compressible Neo-Hookean problem wherein a rigid sphere penetrates a plate which undergoes damage. The results are compared with those presented by Ostwald et al. (2019).

3.1. Quasi-incompressibility: Block under compression

In this example, the UMAT is compared against a three-field formulation using the case of a block under compression. The results of the three-field formulation are extracted from Kadapa and Hossain (2022) following a Neo-Hookean material model having the following strain energy density.

$$\Psi_{\text{loc}} = \frac{\mu}{2}[\bar{I}_1 - 3] + \frac{K}{2}[\ln(J)]^2 \tag{35}$$

The corresponding second Piola stress is defined as

$$\mathbf{S} = \mu J^{-2/3} \left[\mathbb{I} - \frac{1}{3}\mathbf{C}^{-1} \otimes \mathbf{C} \right] : \mathbf{I} + K\ln(J)\mathbf{C}^{-1} \tag{36}$$

A quarter of the block is modelled using appropriate boundary conditions via its symmetry. Fig. 2(a) represents the part of unit dimensions modelled in ABAQUS. The numerical tests are carried out using two different pressure values; 320 MPa and 160 MPa applied in the area marked in the sketch. The Young's modulus is taken as $E = 240.565$ MPa and the quasi-incompressibility of the problem is ensured by setting the Poison's ratio $\nu = 0.4999$. Damage progression is disabled in UMAT for this example. The deformed configuration of the block for a pressure value of 320 MPa is illustrated in the Fig. 2(b). Further, the maximum vertical displacement referred to as compressibility is shown in Fig. 2(c) against four different mesh sizes illustrating good convergence. The hybrid coupled temperature–displacement element C3D8HT is used here and the results show good agreement with that of the three-field formulation presented in Kadapa and Hossain (2022).
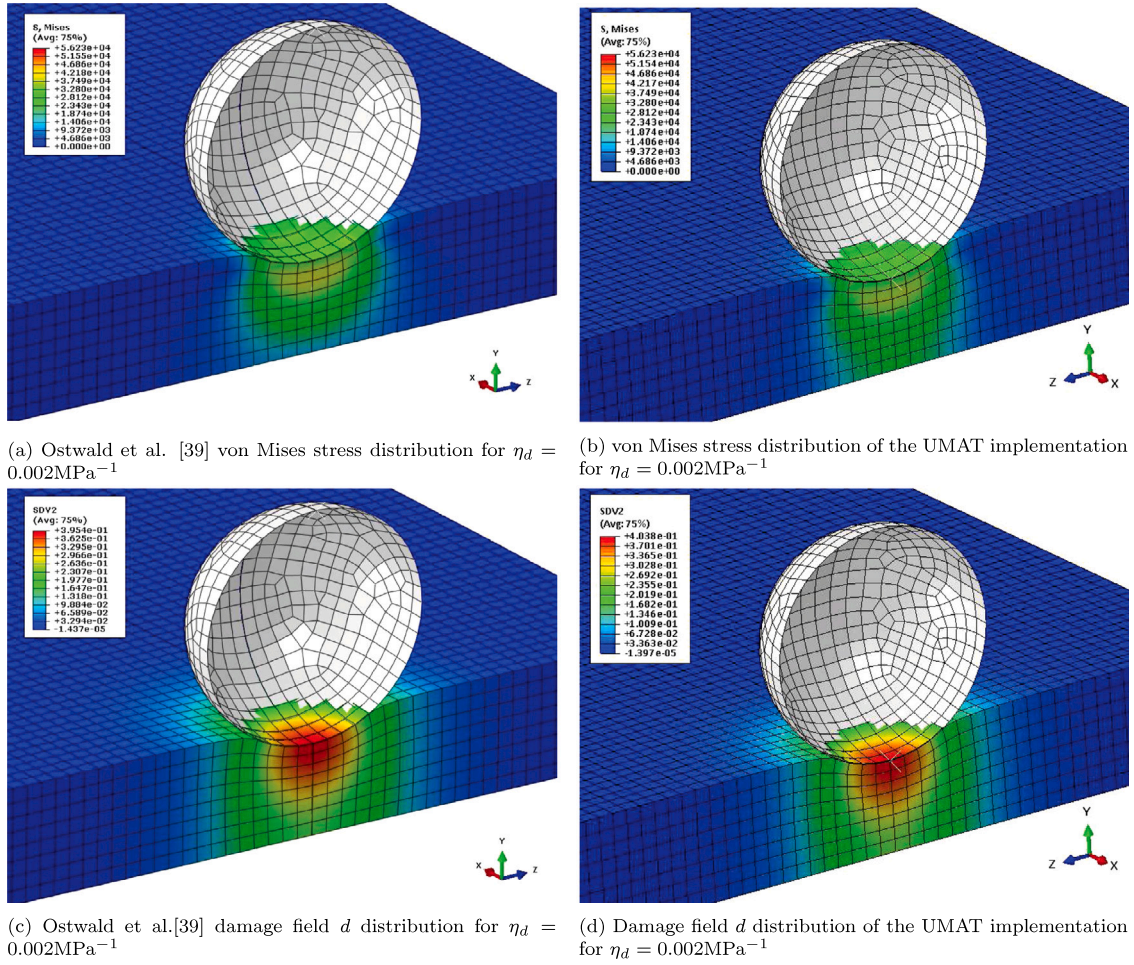
(a) Ostwald et al. [39] von Mises stress distribution for $\eta_d = 0.002\text{MPa}^{-1}$

(b) von Mises stress distribution of the UMAT implementation for $\eta_d = 0.002\text{MPa}^{-1}$

(c) Ostwald et al.[39] damage field d distribution for $\eta_d = 0.002\text{MPa}^{-1}$

(d) Damage field d distribution of the UMAT implementation for $\eta_d = 0.002\text{MPa}^{-1}$

Fig. 4. Comparison of the contour plots of von Mises stress and damage field d with that of Ostwald et al. (2019). Here the damage field d is stored as SDV2 in the UMAT implementation.

3.2. Nonlocal damage model: Contact problem

In this example, a plate indentation test is simulated where a rigid sphere penetrates a specimen undergoing damage. A rectangular block of dimension 200 mm × 100 mm × 15 mm is indented with a rigid sphere. A quarter of the geometry is modelled with symmetric boundary conditions, using 10,000-C3D8T coupled temperature–displacement elements. The sphere is set to penetrate the plate by 3.3 mm and a frictionless boundary is used between them. The Young's modulus and Poison's ratio are 210 GPa and 0.3 respectively. A compressible Neo-Hookean material model is here.

$$\Psi_{\text{loc}} = f(k)\left[\frac{\mu}{2}[I_1 - 3] - \mu\ln(J) + \frac{\lambda}{2}[\ln(J)]^2\right] \quad (37)$$

where, the Lame's constants are given by $\lambda = \dfrac{E\nu}{[1+\nu][1-2\nu]}$ and $\mu = \dfrac{E}{2[1+\nu]}$. The corresponding second Piola stress is defined as

$$\mathbf{S} = f(k)\left[\mu[\mathbf{I} - \mathbf{C}^{-1}] + \lambda\ln(J)\mathbf{C}^{-1}\right] \quad (38)$$

Fig. 3 represents a comparison of the normalised reaction force versus indentation depth plot for the current UMAT and the Ostwald et al. (2019) results. The plot shows good agreement for undamaged and damaged cases ($\eta_d = 0.002$ MPa^{-1}). Further, Fig. 4 illustrates the contour plots of von Mises stress and damage variable d in the deformed configuration. The damage contours of both Ostwald's and the

current UMAT implementations match showing the maximum damage values of 39.54% and 40.38%, respectively. Further, the simulation result shows a von Mises stress of 39.7 GPa which is comparable to that of Ostwald's results. Thus the two examples illustrated confirm the efficacy of the gradient enhanced nonlocal damage model implemented in the UMAT.

4. Damage analysis for selected FlexWECs

The extreme loads encountered by a wave energy device is largely a result of the wave conditions and subsequent hydrodynamic loads on the structure. The structural response of a WEC is influenced by the control system and tuning of the device, i.e., the Power Take-Off (PTO) system. For a rigid-body structure, the device typically enters a survival state whereby the device locked or with minimal movement where the hydrostatic stiffness is increased significantly. The load concentrates about a point, e.g. the hinge between two moving bodies, resulting in a high stress concentration and a potential fatigue failure. An analysis here may utilise traditional accumulative damage laws (Zurkinden et al., 2013; Ambühl et al., 2015), and fracture mechanics approaches (Shittu et al., 2021).

In comparison, a pressurised FlexWEC can be deflated to minimise loading to enter its survivability state. Therefore, the highest loads are more likely to occur in operation, hence an *'extreme state'* here is referred to when the structure is the furthest away from its initial equilibrium position coinciding with the maximum force applied. By
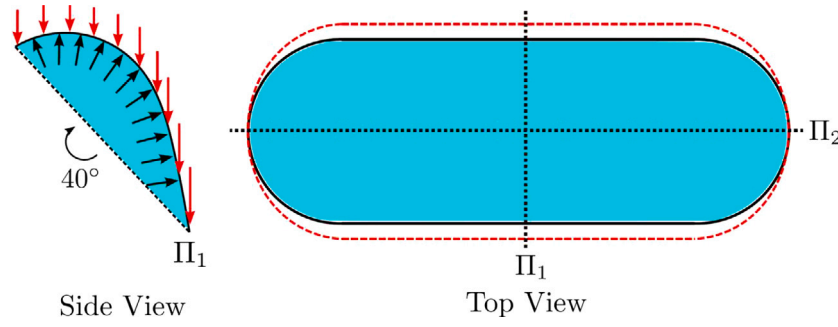
Fig. 5. Hydrostatic boundary conditions for a stadium membrane geometry. Here Π_1 and Π_2 represent the cutting plane normal to the top view of the membrane passing through the corresponding dotted lines shown. The outline of the membrane thus obtained is referred to as Π_1 and Π_2 splines respectively.
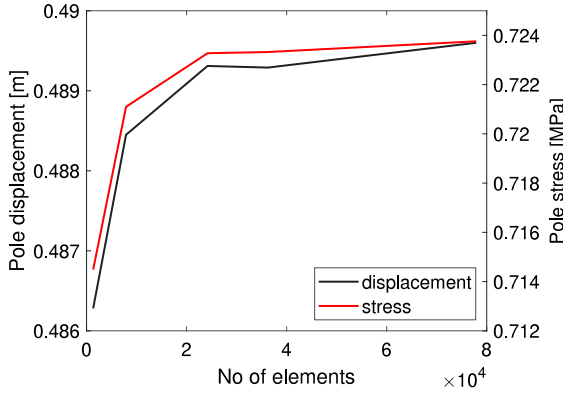

Fig. 6. Mesh convergence results for stadium geometry using C3D8HT elements. The number of elements of 36270 shows good convergence and is adopted in the following studies.

considering the classification for flexible wave energy converters as proposed in Collins et al. (2021), two case studies are analysed here: a submerged air-filled stadia membrane and a water filled near-surface cylindrical tube. These membrane-based FlexWECs respond to loading through changes in deformed shape. Since the designs presented in this section are pressurised volumes, the working fluid is controlled via a pressure regulator. Therefore, these analyses are pressure controlled to achieve the deformation modes under the external hydrostatic conditions. In reality, it is expected that the nonlinearities of the surrounding fluid would play a significant part in the external hydrodynamics and the subsequent deformed shape, however, this is beyond the scope of the current investigation. As the membrane occupies different deformed shapes and the stress is dispersed over a wide area, the crack growth occurs in more of a diffused sense with micro-void formation occurring all over the membrane surface. The severity of the crack formation is witnessed as a reduction in the stress following the classic continuum damage theory of Lemaitre and Chaboche (1990). The nonlocal aspect of the model presented in Section 2 allows for an understanding of the non-homogeneous softening as a result of micro-softening and how this influences the structural behaviour of the device. The effects of softening are twofold: firstly it changes the limit point of the structure, i.e., the point at which structure will fail. Secondly, the softening changes the natural frequency and operation parameters of the device. Therefore, it is an important aspect of consideration from a design longevity and energy harvesting perspective.

The stadium and tubular case studies are given in Section 4.1 and Section 4.2, respectively. For each section, the geometry and boundary conditions are presented. Following this, the two analyses are performed, firstly a failure mode analysis illustrating the expected failure when comparing a damaged and undamaged membrane. Secondly, a parametric study is performed whereby, the damage saturation, threshold, and gradient are modified. It should be noted that the membrane

clamping mechanisms in both analyses were simplified. The goal of this study was to see how damage affects the global membrane mechanics.

4.1. Submerged pressure-differential geometry (stadium geometry)

A submerged pressure differential is a device situated on the subsurface, which harvests energy due to induced pressure variations caused by wave motion on the surface. Several devices and concepts exist in the literature proposing flexible membranes as the interface such as the mWave by Bombora (Ryan and Ryan, 2017; Leighton et al., 2021), m3 Wave (McNatt et al., 2014; Babarit et al., 2017), balloon configuration by Kurniawan and Greaves (2016), dual-membrane converter by Milani et al. (2023), and dielectric elastomer WEC by Righi et al. (2021). In these devices, the membrane encloses an air-filled cell which acts as a pneumatic pump corresponding to the wave cycle, either using an air-turbine or dielectric elastomer generator to convert the mechanical energy to electricity. The previous paper by Collins et al. (2023) uses a circular disc angled 40 degrees with pre-strains of 25% and 50%. From the interest of nonlocal damage, different amount of stretch result in different degrees of damage. Therefore, the dimensions of the case study in Collins et al. (2023) is increased longitudinally to create a stadium-shaped membrane resulting in non-equibiaxial strain. The dimensions and boundary conditions are not based on any real-world design and remain fictitious in this study.

4.1.1. Geometry and boundary conditions

This case study employs a stadium-shaped membrane with two planes of symmetry; see Fig. 5 for information on the size and mesh chosen. A pre-strain of 25% is applied in the short axis. To ensure there was no boundary condition related effects, a ring of perimeter elements with no damage applied was included in the analysis which was ignored in the final simulation. In Eq. (39), the membrane pressure is given which is the summation of internal air P_{air} and external hydrostatic pressure P_{hydro} acting over surface S,

$$P_{mem} = \iint_S \left(P_{air} - P_{hydro} \right) dS \tag{39}$$

where the hydrostatic pressure P_{hydro} is a function of water density ρ_w, gravity g and the coordinate system $h(x, y, z)$

$$P_{hydro} = \rho_w g h(x, y, z) \tag{40}$$

The internal air pressure is given based on ideal gas laws, i.e.,

$$P_{air}(t) = \frac{nRT}{V} \tag{41}$$

where n, R and T refer to the number of moles, universal gas constant ($8.31\ \mathrm{JK^{-1}mol^{-1}}$) and temperature (K), respectively. The pressure is imposed and the volume is calculated at each time-step following the triple integration under the membrane surface relative to a reference point h_{ref}

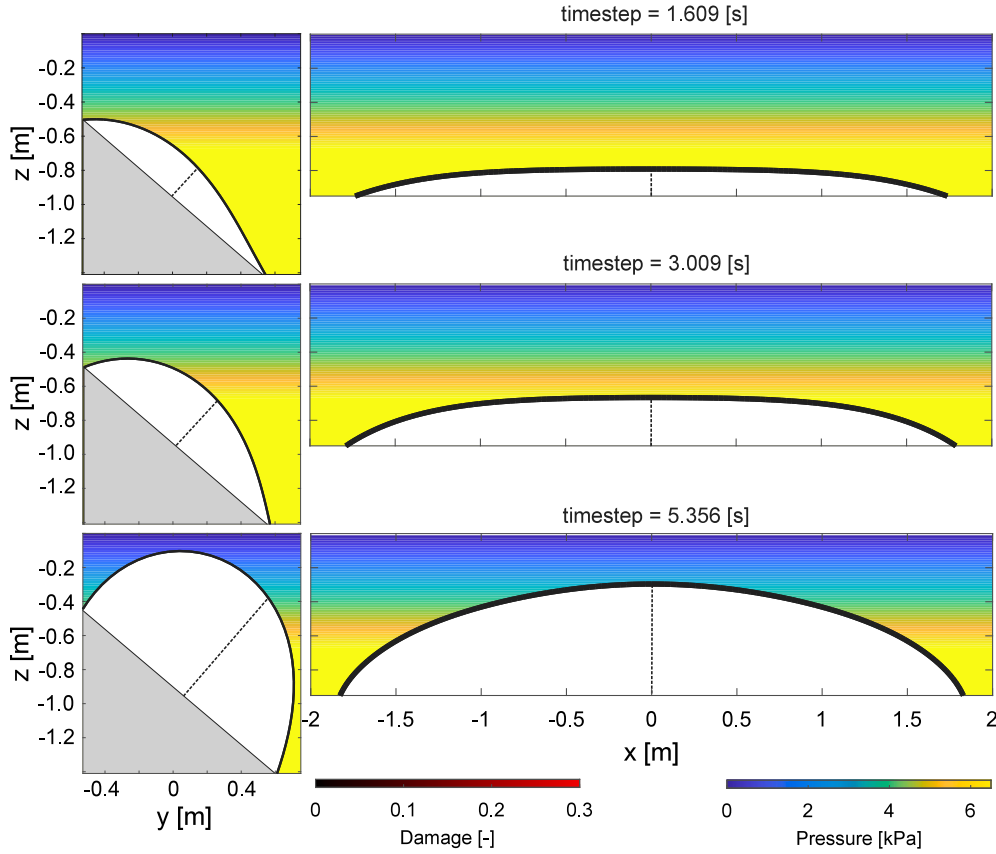$$V = \iiint_V V(h(x, y, z) - h_{ref}) \, dV \tag{42}$$

Fig. 7. Inflation of the stadium membrane using an undamaged Neo-Hookean hyperelastic material. The left and right plots correspond to Π_1 and Π_2 splines, respectively. The inflated shape is plotted for three different load steps, where the z axis corresponds to the depth whereas x and y correspond to the two planar directions.

In a finite element context, this volume may be calculated using the summation of pyramid elements which is given as

$$V \approx \sum_{el}^{n=1} \left(\frac{1}{6} A_{el} h_{el} \right) \tag{43}$$

where A_{el} is the area of the base of the pyramid (membrane surface) and h_{el} is the height of the pyramid from the centroid of the base to the apex which occurs at the reference point located at $\Pi_1 \cap \Pi_2$. After the pre-strain is applied, the air and hydrostatic pressures are applied simultaneously such that $P_{air} - P_{hydro} = 0$, referred to herein as the equilibrium position. For the remaining analysis, the internal pressure is ramped above and below the hydrostatic pressure to simulate the operation of the membrane under quasi-static wave loading conditions. The boundary value problem is solved using finite element analysis in ABAQUS. Fig. 6 illustrates the mesh convergence study for the problem and the final mesh adopted in the following section has a total of 36270-C3D8HT elements with six elements across the thickness to capture the bending behaviour without shear locking.

4.1.2. Failure analysis

To analyse the failure modes of the membrane with and without damage, two models are compared: a Neo-Hookean hyperelastic model and a nonlocal Neo-Hookean damage model. A further parametric study of the nonlocal model is performed in Section 4.1.3. Table 2 shows the parameters selected for the two materials, i.e., the shear and bulk modulus are identical but one has damage and nonlocal aspects. The elastic material properties are adopted from experimental results and the hyperelastic fitting presented in Collins et al. (2023). For the simulations, the independent variable is the pressure, which is ramped above the equilibrium position and is quasi-static with no dynamic effects considered, therefore the flow-rate of inflation is irrelevant in this analysis.

Table 2
Failure analysis comparison between hyperelastic and hyperplastic material parameters.

	μ [MPa]	K [MPa]	η_d[Pa^{-1}]	β_d[Pa^{-1}]	c_d[Pa^{-1}m^2]	κ_d[Pa]
Hyperelastic	0.4	400	–	–	–	–
Hyperplastic	0.4	400	3×10^{-5}	1000	1×10^{-6}	1200

Three figures show the progression of the inflation: Figs. 7 and 8 show the two-dimensional plots corresponding to the Π_1 and Π_2 splines under the hydrostatic pressure field for an undamaged and damaged membrane, respectively. While Fig. 9 shows the pressure–volume function for both materials with timestep marker points corresponding to Fig. 7 and Fig. 8.

The results show some interesting phenomena. The hydrostatic pressure acting on the membrane surface S changes with depth, the membrane accommodates to this change of the pressure by occupying teardrop shape. Both membranes are inflated until failure is reached, where the failure is defined as the point at which the membrane reaches the critical pressure P_{cr} of a limit point instability. At this point there is an abrupt change in the inflation characteristics resulting in a catastrophic failure of the FlexWEC device. When damage is considered, the membrane softens as a result of micro-void formation. As a result, the sensitivity to the pressure-differential changes. As can be seen in Fig. 9, the undamaged membrane can withstand a greater pressure for the same volume of air added compared with a damaged membrane, i.e., 4.4 v. 3 kPa at 1 m^3 and 6.6 v. 4.1 kPa at 1.5 m^3. Additionally, as the inflation progresses the pressure increments for the outward displacement reduces, which occurs until the critical pressure P_{cr} is reached, witnessed as a plateauing of the pressure–volume curve. Due to the limitations of the finite element method, the solution fails to converge beyond this value, an estimate of the expected curve is
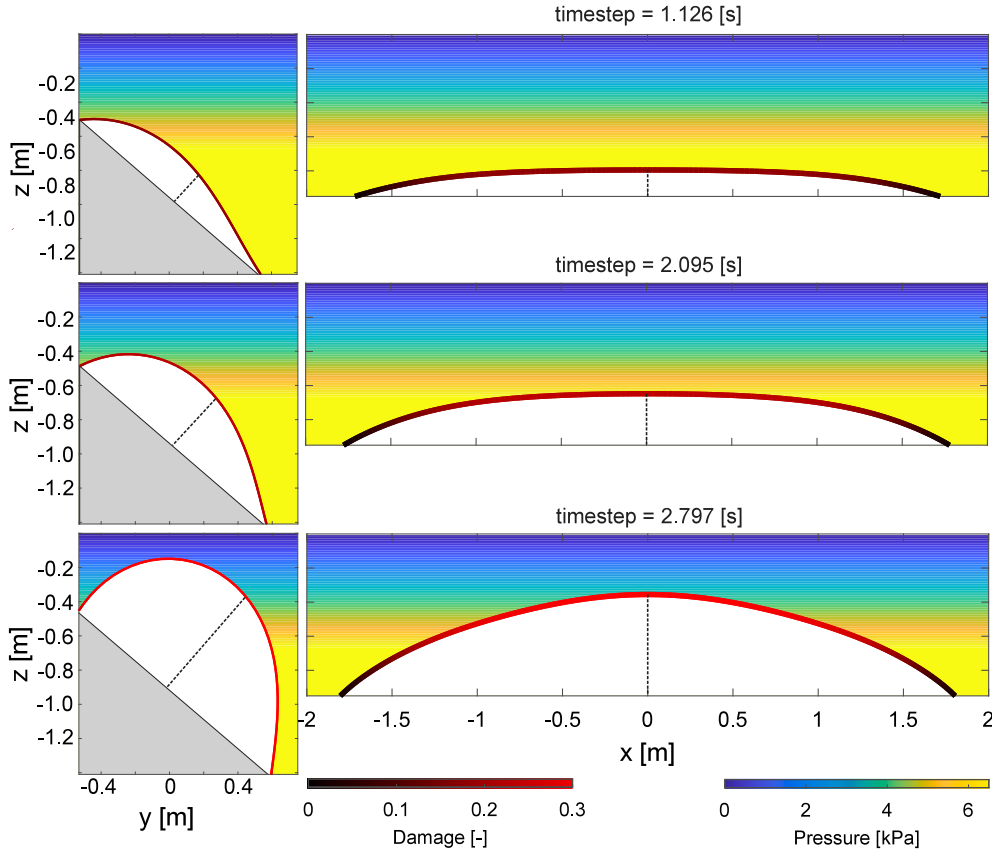
Fig. 8. Inflation of the stadium membrane using the damaged Neo-Hookean hyperelastic material. The left and right plots correspond to Π_1 and Π_2 splines, respectively. The inflated shape is plotted for three different load steps, where the z axis corresponds to the depth and x and y correspond to the two planar directions. Here the extend of damage is plotted using a red colourmap.
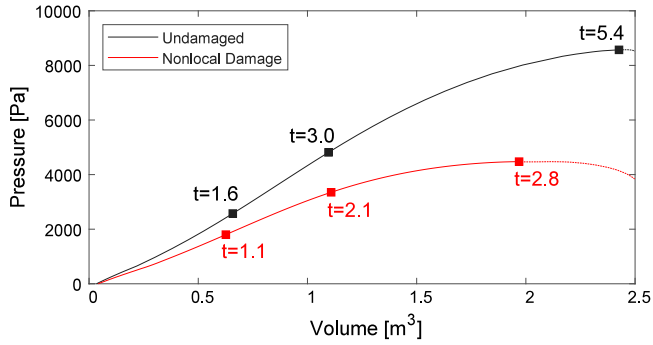

Fig. 9. Pressure–volume function with timestep markers for undamaged and nonlocal damaged membrane material. Here the black and red lines represent the undamaged and damaged material respectively.

Fig. 10. Pressure–volume function for twelve different parameters governing the nonlocal behaviour of the membrane material.

given by the dotted line, whereby the pressure reduces for continued outward displacement. For the damaged membrane, the P_{cr} is lower: 4.5 v. 8.6 kPa, with the volume is also lower at 1.97 v. 2.43 m³. The latter can be explained as a result of the nonlocal aspects of the damage accumulation resulting in a different deformed shape with a lower volume at P_{cr}. This is evident when comparing Fig. 7 and Fig. 8, the membrane occupies a different shape as a result of non-homogeneous softening in the membrane. In Fig. 8, the damage is nearly equal across Π_1 spline, the softening of approximately 30% in this plane is witnessed as a more ovoidal shape due to membrane compensation to the external hydrostatic pressure. The nonlocal aspect of the model is highlighted along the Π_2 spline with a damage differential of 30% to 0%, i.e. no
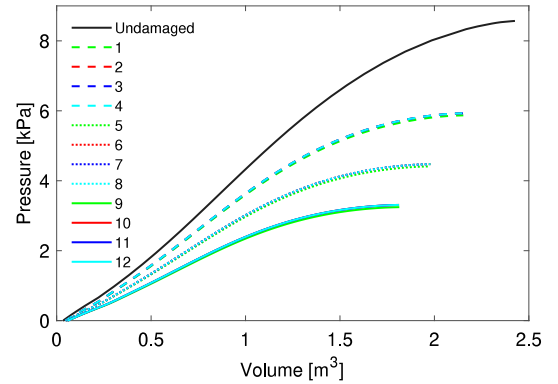
damage occurring at extreme ends of the membrane. As a result, the membrane has pronounced softening along the centre portion resulting in a more pyramidal shape, which encompasses a lower volume of air when compared to the more bulbous shape in Fig. 7.

4.1.3. Influence of nonlocal damage parameters

In this section, twelve different studies are performed to assess the influence of various nonlocal material parameters on the performance of the membrane. Three values of $\eta_d = [2 \times 10^{-5}, 3 \times 10^{-5}, 4 \times 10^{-5}] \text{Pa}^{-1}$ in combination with two values of $\beta_d = [1000, 1] \text{Pa}^{-1}$, $c_d = [1 \times$
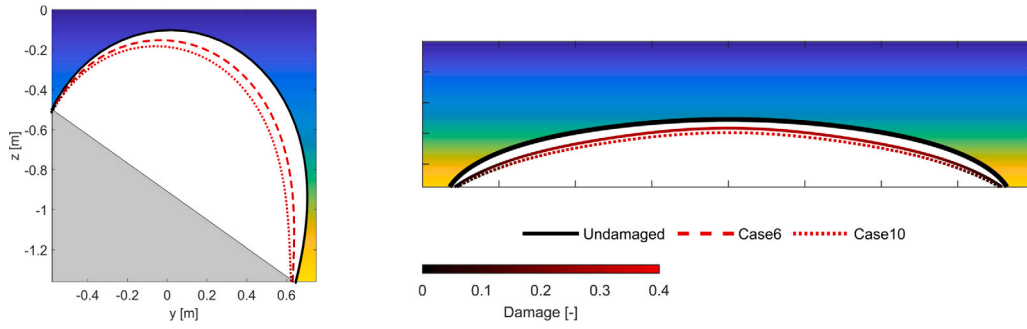
Fig. 11. Illustration of the effect of damage for Case6 and Case10 as compared to the undamaged membrane. The left and right plots correspond to the Π_1 and Π_2 splines respectively. All the membranes are plotted at the instant of instability.

Table 3
Material properties considered in the parametric study.

Case	μ [MPa]	K [MPa]	η_d[Pa^{-1}]	β_d[Pa^{-1}]	c_d[Pa^{-1}m^2]	κ_d[Pa]
Undamaged	0.4	400	–	–	–	–
1	0.4	400	2×10^{-5}	1000	1×10^{-6}	800
2	0.4	400	2×10^{-5}	1000	1×10^{-6}	1200
3	0.4	400	2×10^{-5}	1	1×10^{-6}	1200
4	0.4	400	2×10^{-5}	1000	1	1200
5	0.4	400	3×10^{-5}	1000	1×10^{-6}	800
6	0.4	400	3×10^{-5}	1000	1×10^{-6}	1200
7	0.4	400	3×10^{-5}	1	1×10^{-6}	1200
8	0.4	400	3×10^{-5}	1000	1	1200
9	0.4	400	4×10^{-5}	1000	1×10^{-6}	800
10	0.4	400	4×10^{-5}	1000	1×10^{-6}	1200
11	0.4	400	4×10^{-5}	1	1×10^{-6}	1200
12	0.4	400	4×10^{-5}	1000	1	1200

$10^{-6}, 1]$Pa^{-1}m^2 and $k_d = [800, 1200]$Pa are used. Table 3 lists the combinations of these material properties considered in the study. Fig. 10 illustrates the evolution of the pressure–volume relation corresponding to each parameter. As already established in the previous section, there is a clear reduction in the P_{cr} and volume at failure indicating a reduction in the pressure enduring capacity of the membrane as damage accumulates. Consequently, the influence of nonlocal damage parameters is studied in detail here. From Fig. 10, it can be inferred that both β_d and c_d have negligible influence on P_{cr} for all the values of η_d. However, k_d has a slight influence, showing a small reduction in P_{cr} for Case1, Case5 and Case9 while η_d is fixed. This is inline with the damage formulation as a lower value of k_d leads to an early onset of damage resulting in a lower P_{cr}. On the contrary, η_d has the biggest influence on the pressure–volume relation. A P_{cr} of 8.6 kPa at undamaged state is reduced to roughly 6 kPa, 4.5 kPa, and 3.25 kPa for η_d values if $2 \times 10^{-5}, 3 \times 10^{-5}, 4 \times 10^{-5}$Pa^{-1}, respectively. A higher value of η_d leads to a faster saturation of damage resulting in an earlier instability of the membrane.

Fig. 11 illustrates the inflated states of membranes corresponding to the undamaged state, Case6, and Case10. Here, the membrane plotted in solid black corresponds to the undamaged case and the ones plotted in the dotted line correspond to the two damaged cases. The superposed figure compares the effect of damage on the shape and size of the membrane in Π_1 and Π_2 splines, respectively. As shown in Fig. 10, there is a reduction in the volume enclosed due to the accumulation of damage. The membranes reaches a damage level of 40% and 30% for Case6 and Case10, respectively. Moreover, both the damaged membranes exhibit a slight difference in shape as discussed in Section 4.1.2. Fig. 12 shows the damage contour plot corresponding to the undamaged state and Case1 to Case12. Similar to that of the pressure–volume relation, η_d has the most significant influence on the damage profile of the membrane. Case1 to Case4 experience a damage level of roughly 20% irrespective of the value of β_d, c_d and k_d. However, the damage values

are increased to 30% and 40% for η_d values of 3×10^{-5} and 4×10^{-5}Pa^{-1}, respectively. Moreover, it is also observed that the degradation happens over a large portion at the centre of the membrane irrespective of the damage regularisation parameters. This could be due to the fact that the damage energy release rate is almost constant in the central portion of the membrane as the strain energy density remains the same due to membrane action.

4.2. Attenuator (cylindrical tube geometry)

An attenuator is a device located near the surface orientated perpendicular to the wave crest. The use of a tubular membrane using the so-called 'bulge wave' theory presented by Lighthill (2001) has been an active field of research recently. Several devices exist such as the Anaconda (Farley and Rainey, 2011; Farley et al., 2012), SBM S3 (Pollack and Jean, 2012; Jean et al., 2012), Electric Eel (Grey and Borthwick, 2014) and NREL's DEEC-Tec cylindrical configuration (Boren and Weber, 2022). The wave travelling alongside the tube transfers energy to an inner fluidic portion resulting in a bulge of pressurised seawater. This grows progressively larger along the length of the tube which can either be harvested through a mechanical or a dielectric elastomer PTO. In recent times, there has been research into both floating air bag (Kurniawan et al., 2017) and floating clam-type (Zheng et al., 2023) wave energy converters. Additionally, the study of floating wave hydrodynamics holds significance for the development of floating membrane structures used in applications involving wave and solar energy harvesting (Michele et al., 2023).

4.2.1. Boundary conditions
The tube length is 200 m, with a diameter and tube thickness of 5.0 m and 0.2 m, respectively. In the first step, the membrane is pressurised to 1 kPa relative to the external fluid. The boundary condition is applied such that a bulge starting from 1 kPa gradually increasing along the length of the tube to mimic the bulge growth (see Fig. 13). The pressure acting the membrane P_{mem} is the summation of static equilibrium P_{stat}, dynamic P_{dyn} and external hydrodynamic P_{hydro} pressure acting on the membrane surface S, i.e.,

$$P_{mem} = \iint_S \left[\left(P_{stat} + P_{dyn} \right) - P_{hydro} \right] dS \tag{44}$$

where P_{dyn} is an idealised case of bulge growth in a tube

$$P_{dyn} = A(t) \sin \left(\frac{\pi l(x)}{x(t)} \right) \tag{45}$$

in which $A(t)$ is the time-dependent amplitude which results in the growth of bulge along the length of the tube, $x(t)$ is the time-dependent centroid coordinate of the bulge and $l(x)$ is the length scale parameter dependent on the centroid coordinate. The membrane displacement is fixed where the bulge starts and is free to contract and expand at
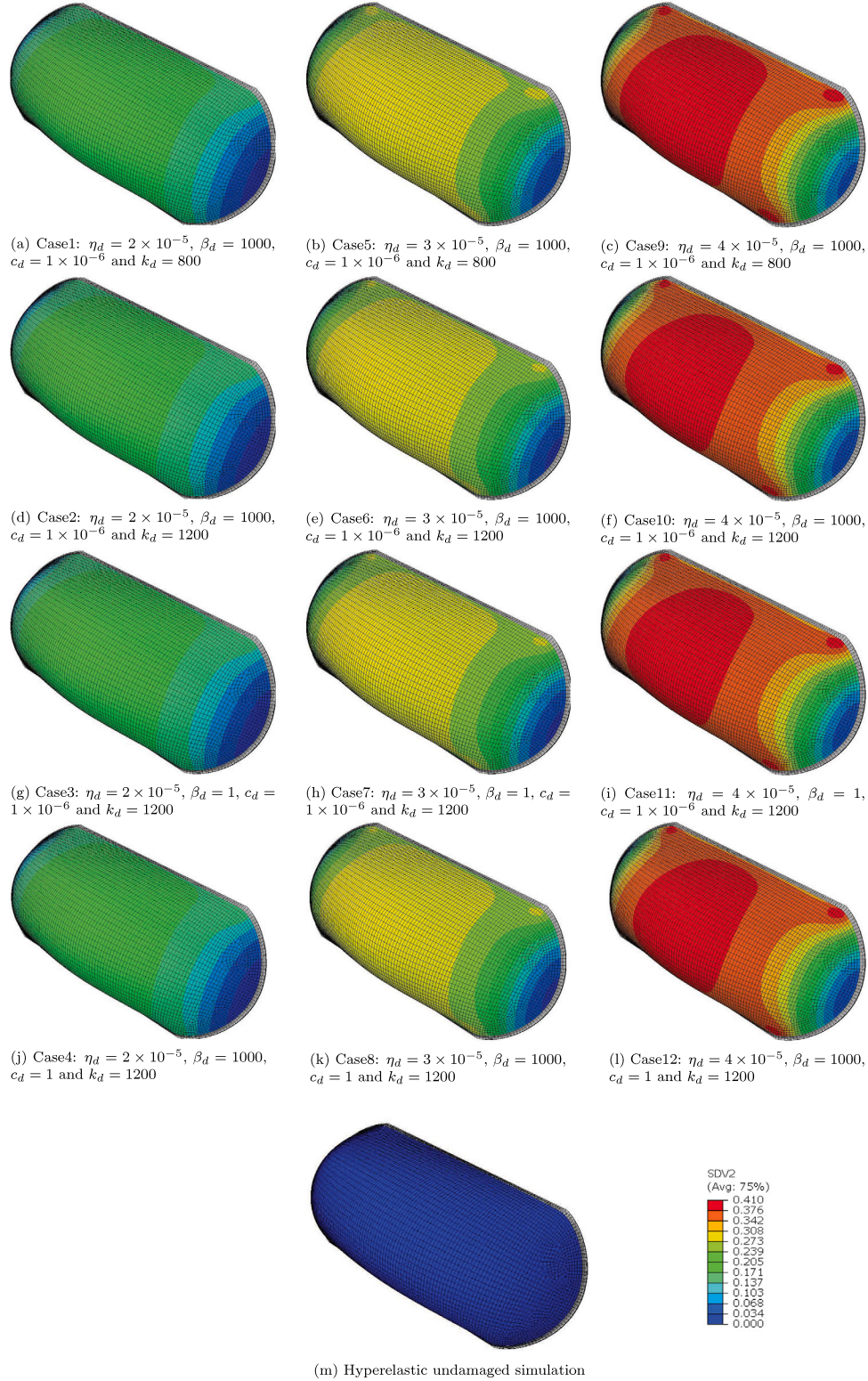
(a) Case1: $\eta_d = 2 \times 10^{-5}$, $\beta_d = 1000$, $c_d = 1 \times 10^{-6}$ and $k_d = 800$

(b) Case5: $\eta_d = 3 \times 10^{-5}$, $\beta_d = 1000$, $c_d = 1 \times 10^{-6}$ and $k_d = 800$

(c) Case9: $\eta_d = 4 \times 10^{-5}$, $\beta_d = 1000$, $c_d = 1 \times 10^{-6}$ and $k_d = 800$

(d) Case2: $\eta_d = 2 \times 10^{-5}$, $\beta_d = 1000$, $c_d = 1 \times 10^{-6}$ and $k_d = 1200$

(e) Case6: $\eta_d = 3 \times 10^{-5}$, $\beta_d = 1000$, $c_d = 1 \times 10^{-6}$ and $k_d = 1200$

(f) Case10: $\eta_d = 4 \times 10^{-5}$, $\beta_d = 1000$, $c_d = 1 \times 10^{-6}$ and $k_d = 1200$

(g) Case3: $\eta_d = 2 \times 10^{-5}$, $\beta_d = 1$, $c_d = 1 \times 10^{-6}$ and $k_d = 1200$

(h) Case7: $\eta_d = 3 \times 10^{-5}$, $\beta_d = 1$, $c_d = 1 \times 10^{-6}$ and $k_d = 1200$

(i) Case11: $\eta_d = 4 \times 10^{-5}$, $\beta_d = 1$, $c_d = 1 \times 10^{-6}$ and $k_d = 1200$

(j) Case4: $\eta_d = 2 \times 10^{-5}$, $\beta_d = 1000$, $c_d = 1$ and $k_d = 1200$

(k) Case8: $\eta_d = 3 \times 10^{-5}$, $\beta_d = 1000$, $c_d = 1$ and $k_d = 1200$

(l) Case12: $\eta_d = 4 \times 10^{-5}$, $\beta_d = 1000$, $c_d = 1$ and $k_d = 1200$

(m) Hyperelastic undamaged simulation

Fig. 12. Damage contour plot at the last converged load step of stadium geometry. Fig. 17(g) to Fig. 12(l) corresponds to Case1 to Case12 and Fig. 12(m) represents the undamaged hyperelastic state.

the other end, allowing for the near incompressibility of the membrane. One-quarter of the membrane is simulated corresponding to the slice obtained by $\Pi_1 \cap \Pi_2$. Similar to the previous example, hybrid coupled temperature–displacement elements are used here. The number of C3D8HT elements was chosen as 18,000 based on the mesh convergence study presented in Fig. 14.
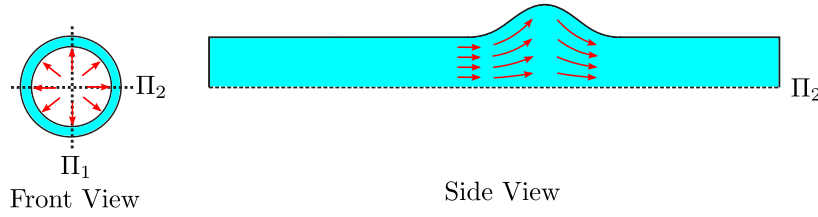
Fig. 13. Hydrostatic boundary conditions for a cylindrical membrane geometry. Here Π_1 and Π_2 represents the two cutting plane normal to the front view passing through the dotted lines shown.
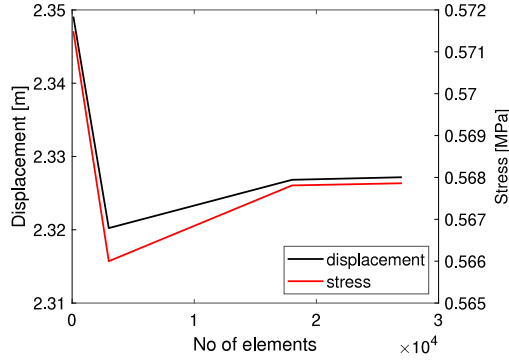

Fig. 14. Mesh convergence results for attenuator using C3D8HT elements. The number of elements of 18,000 shows good convergence.

Table 4
Failure analysis comparison between hyperelastic and damage material parameters.

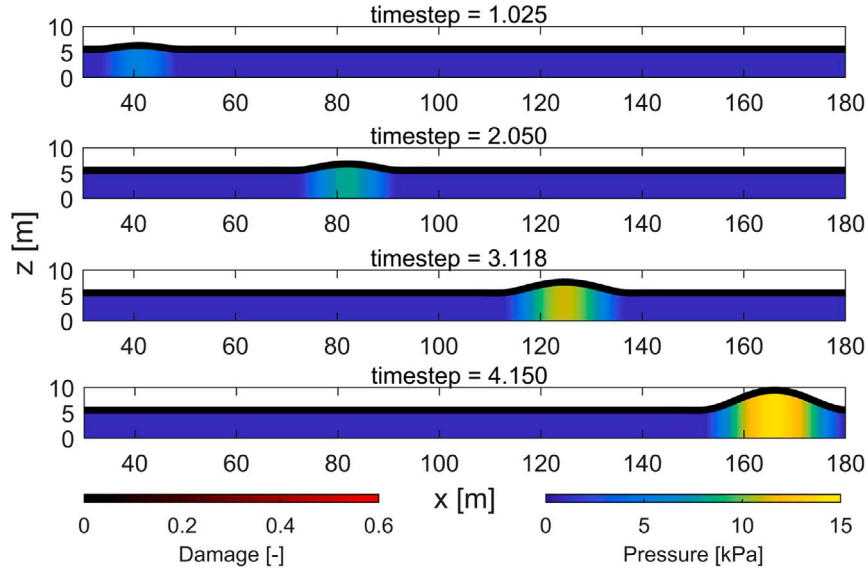| Case	μ [MPa]	K_{bulk} [MPa]	η_d[Pa^{-1}]	β_d[Pa^{-1}]	c_d[Pa^{-1}m^2]	κ_d[Pa]
Hyperelastic	0.4	400	–	–	–	–
1	0.4	400	5 ×10^{-5}	1000	1 ×10^{-6}	100
2	0.4	400	5 ×10^{-5}	1	1 ×10^{-6}	100
3	0.4	400	5 ×10^{-5}	1000	1	100
4	0.4	400	1 ×10^{-4}	1000	1 ×10^{-6}	100
5	0.4	400	1 ×10^{-4}	1	1 ×10^{-6}	100
6	0.4	400	1 ×10^{-4}	1000	1	100
7	0.4	400	2 ×10^{-4}	1000	1 ×10^{-6}	100
8	0.4	400	2 ×10^{-4}	1	1 ×10^{-6}	100
9	0.4	400	2 ×10^{-4}	1000	1	100

4.2.2. Failure analysis

Similarly to the case study presented in Section 4.1.2, two materials, one undamaged and the other damaged are compared under identical boundary conditions. Due to the different scale of the *'Bulge Wave'* FlexWEC as well as different strain duty, different parameters for the nonlocal damage aspects are considered by keeping the elastic properties unchanged, see Table 4 for details. Figs. 15(a) and 15(b) show the outline of the bulge wave travelling through the Attenuator device corresponding to an undamaged and damaged (case1) material. The bulge locations at different time steps are shown here, such that the last time step corresponds to the point of instability. During the initial pressurisation stage, a small amount of damage occurs, as the bulge progresses this damage becomes larger until an aneurysm forms. Here the damaged material results in an early onset of aneurysm compared to the undamaged case. This early onset can be characterised by identifying the location of the aneurysm and the corresponding pressure P_{cr}. The undamaged attenuator undergoes instability at roughly 160 m whereas for the damaged case it occurs at 140 m. A similar reduction in critical pressure from 13 kPa to 12.3 kPa is also observed at a maximum damage value of 15%. Further, Fig. 16 provides the pressure vs radial stretch plot for different cases of material properties listed in Table 4.

Here nine different damage cases are studied to assess the effect of various nonlocal damage parameters. Three values of η_d = [5 × 10^{-5}, 1 × 10^{-4}, 2 × 10^{-4}]Pa^{-1} in combination with two values of β_d =
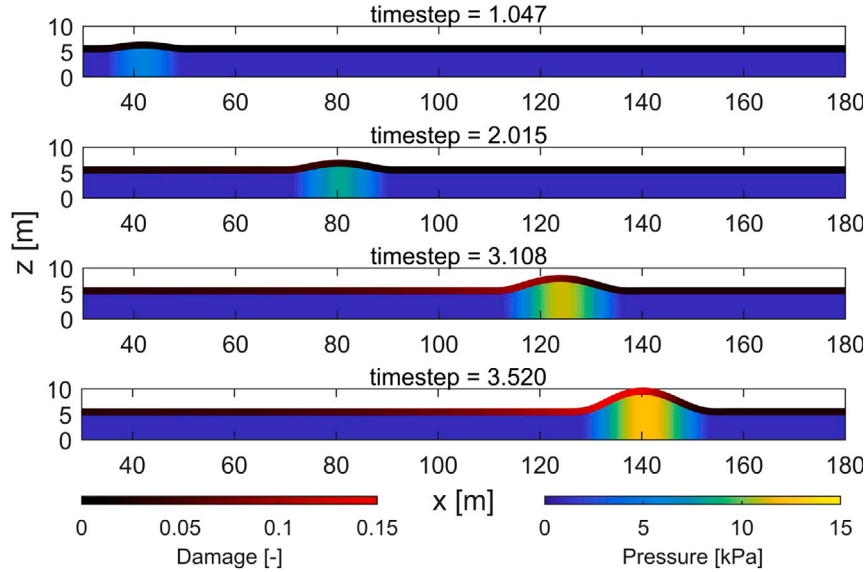
[1000, 1]Pa^{-1}, c_d = [1 × 10^{-6}, 1]Pa^{-1}m^2 and k_d = 100Pa are used. Contrary to the stadium membrane, the displacement/radial stretch at failure is almost invariable showing a maximum variation of only 2.1%. All the cases presented in Fig. 16 show a failure stretch in the range of 1.86–1.9 and the corresponding displacements of 4.3 m to 4.5 m. Similar to the stadium geometry, η_d has the biggest influence on P_{cr}. However, the damage regularisation parameter c_d has a direct influence on P_{cr} compared to the penalty parameter β_d. This influence is more pronounced for higher values of η_d. i.e. for $\eta_d = 5 \times 10^{-5}$Pa^{-1}, a change in c_d from 1×10^{-6} to 1Pa^{-1}m^2 results in a 2.6% increase in P_{cr}. However, this difference becomes 7.8% and 13% for $\eta_d = 1 \times 10^{-4}$Pa^{-1} and 2×10^{-5}Pa^{-1} for the same change in c_d. This is because an increase in c_d results in a more diffused damage profile resulting in a higher load carrying capacity. Fig. 17 clearly illustrates this effect where the damage contour is plotted on a cut section of the tube showing its internal surface. The damage profile is diffused upstream of the bulge wave resulting in a more uniform damage distribution for higher values of c_d. However, for smaller values of c_d the damage is more concentrated on the downstream side of the wave. This effect is more physical as the bulge wave moves along the length of the tube, the material on its upstream side is always in pristine condition (if the effects of initial pressurisation are ignored) compared to that on the downstream side where there is already some damage accumulated from the previous loadstep. Hence the choice of c_d becomes critical to capture the behaviour of the device. The figure also suggests that for higher values of η_d (cases 3–9), the tube undergoes more damage during the initial pressurisation stage as opposed to smaller values (cases 1–3) where the bulk of the tube is nearly undamaged.

5. Conclusion

The present study investigated the response of two different types of FlexWECs made from rubber-like materials. These devices include a submerged air-filled membrane operating on the pressure differential principle and a near surface water-filled tube operating on the bulge wave principle. The simulations assumed a quasi-static condition which enabled the modelling of both the membrane devices at their equilibrium state by neglecting the hydrodynamic effects. This simplification facilitated a faster computation of results but at the expense of accuracy of a fully coupled multiphysics analysis. However, the goal of this paper was to understand the effect of damage accumulation on the membrane response. To achieve this goal, the constitutive modelling was done based on a Neo-Hookean hyperelastic material in conjunction with nonlocal gradient-enhanced damage modelling. This approach enabled the study of the softening effects in the membrane material caused by micro-void formations. A parametric study was performed to understand the effects of different nonlocal material parameters on the performance of both devices. The findings revealed that the most significant influence on the critical pressure of both devices came from the damage saturation parameter (η_d). However, the damage regularisation parameters namely c_d and β_d had negligible effects on the performance of air-filled membranes. Contrary to other crack propagation problems, the stadium membrane experiences a similar level of material softening throughout the whole structure since the stress differential is small due to membrane action. Consequently, the nonlocal aspects of the model

(a) Inflation of attenuator for an undamaged Neo-Hookean hyperelastic material.

(b) Inflation of Attenuator for a damaged Neo-Hookean hyperelastic material(case1)

Fig. 15. The results of attenuator inflation corresponding to four different timesteps are presented here when the bulge wave moves from left to right of the tube. The vertical axis is marked as z showing the height of the bulge wave and the length of the tube is marked along x direction. The internal pressure leading to the bulge wave motion and the corresponding damage is illustrated using two separate colorbars as marked.
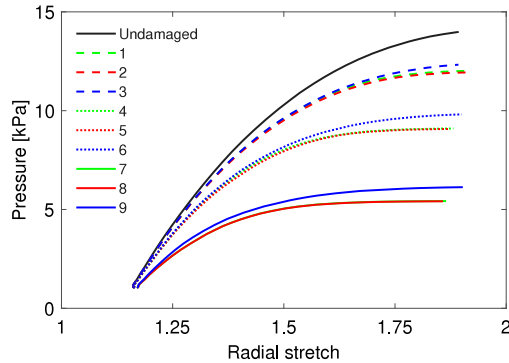

Fig. 16. Pressure vs stretch diagram for attenuator corresponding to the undamaged and damaged hyperelastic materials.

are relatively small and have little effect on the overall membrane response. The damage saturation parameter still influences the critical pressure of the membrane. However, for the attenuator device, the damage regularisation parameter c_d influences the diffusion of damage in the material such that a higher value of c_d leads to an undesirable distribution of damage in the membrane. Furthermore, it was also observed that both the devices at the limit state do not fully degrade. In future, this model can be extended account for other physical mechanisms such as viscoelasticity and in-silico fatigue damage using a cyclic counting algorithm. The case studies presented herein represent relatively low changes in stretch and due to membrane action: a low degree of stress variation. However, Direct Generation or DEEC-Tec designs are expected to exhibit much higher strains and potentially utilise auxetic structures. These designs will make for interesting future case studies along with the incorporation of electro-mechanical fatigue.
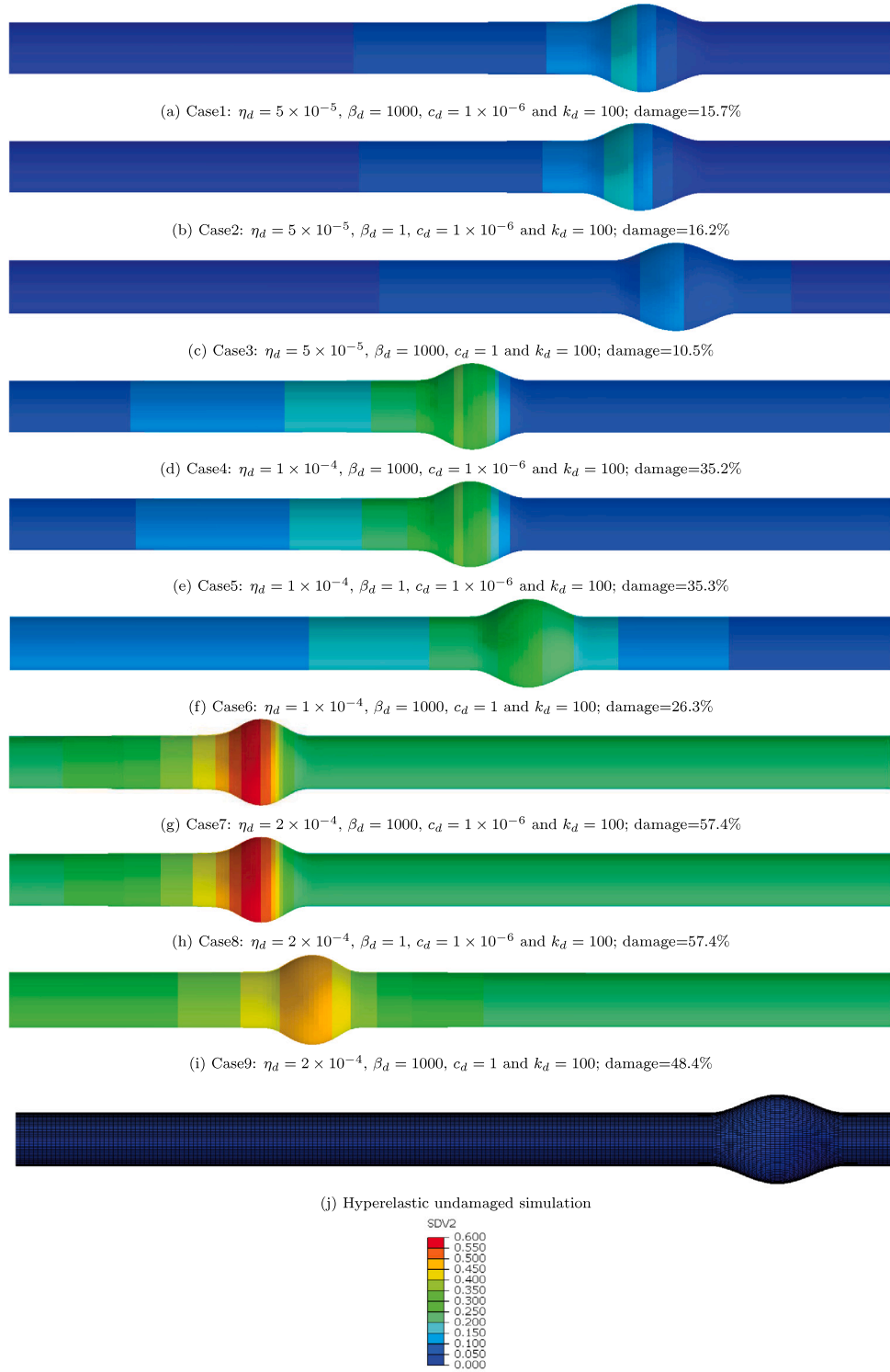
(a) Case1: $\eta_d = 5 \times 10^{-5}$, $\beta_d = 1000$, $c_d = 1 \times 10^{-6}$ and $k_d = 100$; damage=15.7%

(b) Case2: $\eta_d = 5 \times 10^{-5}$, $\beta_d = 1$, $c_d = 1 \times 10^{-6}$ and $k_d = 100$; damage=16.2%

(c) Case3: $\eta_d = 5 \times 10^{-5}$, $\beta_d = 1000$, $c_d = 1$ and $k_d = 100$; damage=10.5%

(d) Case4: $\eta_d = 1 \times 10^{-4}$, $\beta_d = 1000$, $c_d = 1 \times 10^{-6}$ and $k_d = 100$; damage=35.2%

(e) Case5: $\eta_d = 1 \times 10^{-4}$, $\beta_d = 1$, $c_d = 1 \times 10^{-6}$ and $k_d = 100$; damage=35.3%

(f) Case6: $\eta_d = 1 \times 10^{-4}$, $\beta_d = 1000$, $c_d = 1$ and $k_d = 100$; damage=26.3%

(g) Case7: $\eta_d = 2 \times 10^{-4}$, $\beta_d = 1000$, $c_d = 1 \times 10^{-6}$ and $k_d = 100$; damage=57.4%

(h) Case8: $\eta_d = 2 \times 10^{-4}$, $\beta_d = 1$, $c_d = 1 \times 10^{-6}$ and $k_d = 100$; damage=57.4%

(i) Case9: $\eta_d = 2 \times 10^{-4}$, $\beta_d = 1000$, $c_d = 1$ and $k_d = 100$; damage=48.4%

(j) Hyperelastic undamaged simulation

Fig. 17. Damage contour plot at the last converged timestep of attenuator geometry. Fig. 17(a) to Fig. 17(i) corresponds to Case1 to Case9 and Fig. 17(j) represents the undamaged hyperelastic state.

CRediT authorship contribution statement

Deepak George: Writing – original draft, Analysis, Implementation, Simulation. **Ieuan Collins:** Writing – original draft, Analysis, Implementation, Simulation. **Ian Masters:** Editing, Analysis, Supervision. **Mokarram Hossain:** Conceptualization, Writing – original draft, Editing, Supervision.

Declaration of competing interest

The authors declare that they have no known competing financial interests or personal relationships that could have appeared to influence the work reported in this paper.

Data availability

No data was used for the research described in the article.

Acknowledgements

References

Abad, F., Dai, S., Zhao, G., Alarcon, G., Yang, L., Huang, Y., Xiao, Q., Brennan, F., 2023. Experimental study on inflatable circular diaphragms used in the oscillating water column wave energy converter. In: Lotfian, S. (Ed.), Advances in the Analysis and Design of Marine Structures. Vol. 11, first ed. CRC Press.

Ambühl, S., Ferri, F., Kofoed, J.P., Sørensen, J.D., 2015. Fatigue reliability and calibration of fatigue design factors of wave energy converters. Int. J. Mar. Energy 10, 17–38.

Anon, 2021. Abaqus theory guide. URL https://help.3ds.com/2021/english/dssimulia_established/simacaetherefmap/simathe-c-hyperelastic.htm?contextscope=all.

Anon, 2023a. Direct generation concept design competition. https://www.waveenergyscotland.co.uk/programmes/details/next-generation-wave-energy-direct-distributed-flexible/direct-generation-concept-design-competition/. (Accessed 2 November 2023).

Anon, 2023b. Distributed embedded energy converter technologies. https://www.nrel.gov/water/distributed-embedded-energy-converter-technologies.html. (Accessed 2 November 2023).

Anon, 2023c. DOE launches prize to harness the power of ocean waves with new technologies. https://www.energy.gov/eere/water/articles/doe-launches-prize-harness-power-ocean-waves-new-technologies. (Accessed 2 November 2023).

Anon, 2023d. Next generation wave energy, wave energy Scotland. https://www.waveenergyscotland.co.uk/programmes/details/next-generation-wave-energy-direct-distributed-flexible/. (Accessed 2 November 2023).

Babarit, A., 2018. Ocean Wave Energy Conversion: Resource, Technologies and Performance. ISTE Press and Elsevier, UK.

Babarit, A., Wendt, F., Yu, Y.-H., Weber, J., 2017. Investigation on the energy absorption performance of a fixed-bottom pressure-differential wave energy converter. Appl. Ocean Res. 65, 90–101.

Bažant, Z.P., Jirásek, M., 2002. Nonlocal integral formulations of plasticity and damage: Survey of progress. J. Eng. Mech. 128 (11), 1119–1149.

Bažant, Z.P., Pijaudier-Cabot, G., 1988. Nonlocal continuum damage, localization instability and convergence. J. Appl. Mech. 55 (2), 287–293.

Bonet, J., Wood, R., Mahaney, J., Heywood, P., 2000. Finite element analysis of air supported membrane structures. Comput. Methods Appl. Mech. Engrg. 190 (5), 579–595. http://dx.doi.org/10.1016/S0045-7825(99)00428-4, URL https://www.sciencedirect.com/science/article/pii/S0045782599004284.

Boren, B.C., Weber, J., 2022. Flexible wave energy converter. Google Patents. US Patent 11, 401, 910.

Clément, A., McCullen, P., ao, A.F., Fiorentino, A., Gardner, F., Hammarlund, K., Lemonis, G., Lewis, T., Nielsen, K., Petroncini, S., Pontes, M.-T., Schild, P., Sjöström, B.-O., Sørensen, H.C., Thorpe, T., 2002. Wave energy in Europe: current status and perspectives. Renew. Sustain. Energy Rev. 6 (5), 405–431. http://dx.doi.org/10.1016/S1364-0321(02)00009-6, URL https://www.sciencedirect.com/science/article/pii/S1364032102000096.

Coelho, M., Roehl, D., Bletzinger, K.-U., 2014. Numerical and analytical solutions with finite strains for circular inflated membranes considering pressure–volume coupling. Int. J. Mech. Sci. 82, 122–130. http://dx.doi.org/10.1016/j.ijmecsci.2014.03.012, URL https://www.sciencedirect.com/science/article/pii/S0020740314000885.

Collins, I., Contino, M., Marano, C., Masters, I., Hossain, M., 2023. On the influence of time-dependent behaviour of elastomeric wave energy harvesting membranes using experimental and numerical modelling techniques. Eur. J. Mech. A Solids 98, 104895. http://dx.doi.org/10.1016/j.euromechsol.2022.104895, URL https://www.sciencedirect.com/science/article/pii/S0997753822003254.

Collins, I., Hossain, M., Dettmer, W., Masters, I., 2021. Flexible membrane structures for wave energy harvesting: A review of the developments, materials and computational modelling approaches. Renew. Sustain. Energy Rev. 151, 111478.

Dal, H., Gültekin, O., Başdemir, S., Açan, A.K., 2022. Ductile-brittle failure of amorphous glassy polymers: A phase-field approach. Comput. Methods Appl. Mech. Engrg. 401, 115639. http://dx.doi.org/10.1016/j.cma.2022.115639, URL https://www.sciencedirect.com/science/article/pii/S0045782522005941.

de Borst, R., Pamin, J., 1996. Some novel developments in finite element procedures for gradient-dependent plasticity and finite elements. Int. J. Numer. Methods 39, 477–2505.

de Borst, R., Verhoosel, C.V., 2016. Gradient damage vs phase-field approaches for fracture: Similarities and differences. Comput. Methods Appl. Mech. Engrg. 312, 78–94. http://dx.doi.org/10.1016/j.cma.2016.05.015, URL https://www.sciencedirect.com/science/article/pii/S0045782516303796. Phase Field Approaches to Fracture.

de Souza Neto, E., Perić, D., Dutko, M., Owen, D., 1996. Design of simple low order finite elements for large strain analysis of nearly incompressible solids. Int. J. Solids Struct. 33 (20), 3277–3296. http://dx.doi.org/10.1016/0020-7683(95)00259-6.

Denli, F.A., Gültekin, O., Holzapfel, G.A., Dal, H., 2020. A phase-field model for fracture of unidirectional fiber-reinforced polymer matrix composites. Comput. Mech. 65, 1149–1166. http://dx.doi.org/10.1007/s00466-019-01812-1.

Dimitrijevic, B.J., Hackl, K., 2007. A method for gradient enhancement of continuum damage models. Techn. Mech. 28 (1), 43–52.

Duranti, M., Righi, M., Vertechy, R., Fontana, M., 2017. A new class of variable capacitance generators based on the dielectric fluid transducer. Smart Mater. Struct. 26 (11), 115014.

Eriksson, A., Nordmark, A., Patil, A., Zhou, Y., 2016. Parametric stability investigations for hydro-statically loaded membranes. Comput. Struct. 174, 33–41. http://dx.doi.org/10.1016/j.compstruc.2015.08.014, URL https://www.sciencedirect.com/science/article/pii/S0045794915002473. CIVIL-COMP.

Eringen, A.A., Wegner, J.R., 2003. Nonlocal continuum field theories. Appl. Mech. Rev. 56 (2), B20–B22. http://dx.doi.org/10.1115/1.1553434, arXiv:https://asmedigitalcollection.asme.org/appliedmechanicsreviews/article-pdf/56/2/B20/5439838/b17_1.pdf.

Esmaeili, A., George, D., Masters, I., Hossain, M., 2023. Biaxial experimental characterizations of soft polymers: A review. Polym. Test. 128, 108246. http://dx.doi.org/10.1016/j.polymertesting.2023.108246, URL https://www.sciencedirect.com/science/article/pii/S0142941823003264.

Farley, F.J.M., Rainey, R.C.T., 2011. Distensible tube wave energy converter. Google Patents. US Patent 7, 980, 071.

Farley, F., Rainey, R., Chaplin, J., 2012. Rubber tubes in the sea. Phil. Trans. R. Soc. A 370 (1959), 381–402.

French, M.J., 1979. Water wave energy conversion device using flexible membranes. Google Patents. US Patent 799, 524.

Grey, S., Borthwick, A., 2014. Apparatus and method for extracting energy from fluid motion. Google Patents. US Patent 8, 633, 608.

Holzapfel, G.A., 2000. Nonlinear Solid Mechanics: A Continuum Approach for Engineering. John Wiley & Sons, UK, URL https://www.ebook.de/de/product/3056011/holzapfel_nonlinear_solid_mechanics.html.

Hossain, M., Steinmann, P., 2013. More hyperelastic models for rubber-like materials: consistent tangent operators and comparative study. J. Mech. Behav. Mater. 22 (1–2), http://dx.doi.org/10.1515/jmbm-2012-0007.

Jean, P., Wattez, A., Ardoise, G., Melis, C., Van Kessel, R., Fourmon, A., Barrabino, E., Heemskerk, J., Queau, J., 2012. Standing wave tube electro active polymer wave energy converter. In: Electroactive Polymer Actuators and Devices (EAPAD) 2012. Vol. 8340. SPIE, pp. 75–95.

Jha, N.K., Nackenhorst, U., Pawar, V.S., Nadella, R., Guruprasad, P., 2019. On the constitutive modelling of fatigue damage in rubber-like materials. Int. J. Solids Struct. 159, 77–89. http://dx.doi.org/10.1016/j.ijsolstr.2018.09.022, URL https://www.sciencedirect.com/science/article/pii/S0020768318303780.

Kachanov, L.M., 1958. Time of the rupture process under creep conditions. Izvestija Akademii Nauk Sojuza Sovetskich Socialisticeskich Respubliki 8, 26–31.

Kadapa, C., 2019. Novel quadratic Bézier triangular and tetrahedral elements using existing mesh generators: Extension to nearly incompressible implicit and explicit elastodynamics in finite strains. Internat. J. Numer. Methods Engrg. 119 (2), 75–104. http://dx.doi.org/10.1002/nme.6042.

Kadapa, C., Dettmer, W., Perić, D., 2016. Subdivision based mixed methods for isogeometric analysis of linear and nonlinear nearly incompressible materials. Comput. Methods Appl. Mech. Engrg. 305, 241–270. http://dx.doi.org/10.1016/j.cma.2016.03.013.

Kadapa, C., Hossain, M., 2022. A linearized consistent mixed displacement-pressure formulation for hyperelasticity. Mech. Adv. Mater. Struct. 29 (2), 267–284. http://dx.doi.org/10.1080/15376494.2020.1762952.

Koh, S.J.A., Keplinger, C., Li, T., Bauer, S., Suo, Z., 2010. Dielectric elastomer generators: How much energy can be converted? IEEE/ASME Trans. Mechatron. 16 (1), 33–41.

Konica, S., Sain, T., 2023. Phase-field fracture modeling for unidirectional fiber-reinforced polymer composites. Eur. J. Mech. A Solids 100, 105035. http://dx.doi.org/10.1016/j.euromechsol.2023.105035, URL https://www.sciencedirect.com/science/article/pii/S0997753823001274.

Krajcinovic, D., Lemaitre, J., 1987. Continuum Damage Mechanics Theory and Applications. Springer Vienna, New York, URL https://doi.org/10.1007/978-3-7091-2806-0.

Kurniawan, A., Chaplin, J.R., Greaves, D.M., Hann, M., 2017. Wave energy absorption by a floating air bag. J. Fluid Mech. 812, 294–320. http://dx.doi.org/10.1017/jfm.2016.811.

Kurniawan, A., Greaves, D., 2016. Wave power absorption by a submerged balloon fixed to the sea bed. IET Renew. Power Gener. 10 (10), 1461–1467.

Lasry, D., Belytschko, T., 1988. Localization limiters in transient problems. Int. J. Solids Struct. 24 (6), 581–597.

Leighton, S., Algie, C., Ryan, S.K., 2021. Wave energy conversion/convertors. Google Patents. US Patent 10, 883, 471.

Lemaitre, J., Chaboche, J.-L., 1990. Mechanics of Solid Materials. Cambridge University Press, UK.

Liebe, T., Steinmann, P., Benallal, A., 2001. Theoretical and computational aspects of a thermodynamically consistent framework for geometrically linear gradient damage. Comput. Methods Appl. Mech. Engrg. 190 (49), 6555–6576. http://dx.doi.org/10.1016/S0045-7825(01)00250-X, URL https://www.sciencedirect.com/science/article/pii/S004578250100250X.

Lighthill, J., 2001. Waves in fluids. Cambridge University Press.

LLC, M., 2022. Wello, clean energy from ocean waves. URL https://wello.eu/.

McNatt, J.C., Özkan-Haller, H.T., Morrow, M., Delos-Reyes, M., 2014. Preliminary modeling and analysis of a horizontal pressure differential wave energy converter. J. Offshore Mech. Arct. Eng. 136 (1), 011901.

Michele, S., Zheng, S., Buriani, F., Borthwick, A.G., Greaves, D.M., 2023. Floating hydroelastic circular plate in regular and irregular waves. Eur. J. Mech. B/Fluids 99, 148–162. http://dx.doi.org/10.1016/j.euromechflu.2023.01.008, URL https://www.sciencedirect.com/science/article/pii/S0997754623000201.

Milani, L., Thorniley, S., Kurniawan, A., Wolgamot, H., 2023. Modelling and testing of a pressure-differential wave energy converter with flexible membranes. Appl. Ocean Res. 134, 103516. http://dx.doi.org/10.1016/j.apor.2023.103516, URL https://www.sciencedirect.com/science/article/pii/S0141118723000573.

Moretti, G., Herran, M.S., Forehand, D., Alves, M., Jeffrey, H., Vertechy, R., Fontana, M., 2020a. Advances in the development of dielectric elastomer generators for wave energy conversion. Renew. Sustain. Energy Rev. 117, 109430.

Moretti, G., Rosset, S., Vertechy, R., Anderson, I., Fontana, M., 2020b. A review of dielectric elastomer generator systems. Adv. Intell. Syst. 2 (10), 2000125.

Mühlhaus, H.B., Alfantis, E.C., 1991. A variational principle for gradient plasticity. Int. J. Solids Struct. 28 (7), 845–857.

Neto, E.A.S., Pires, F.M.A., Owen, D.R.J., 2005. F-bar-based linear triangles and tetrahedra for finite strain analysis of nearly incompressible solids. Part I: formulation and benchmarking. Internat. J. Numer. Methods Engrg. 62 (3), 353–383. http://dx.doi.org/10.1002/nme.1187.

Ostwald, R., Kuhl, E., Menzel, A., 2019. On the implementation of finite deformation gradient-enhanced damage models. Comput. Mech. 64, 847–877. http://dx.doi.org/10.1007/s00466-019-01684-5, URL https://link.springer.com/article/10.1007/s00466-019-01684-5#citeas.

Pamin, J., 1994. Gradient-Dependent Plasticity in Numerical Simulation of Localization Phenomena (Ph.D. thesis). Delft University of Technology, Delft.

Pecher, A., Kofoed, J., 2017. Handbook of Ocean Wave Energy. Springer, UK, http://dx.doi.org/10.1007/978-3-319-39889-1, URL https://link.springer.com/book/10.1007/978-3-319-39889-1.

Peerlings, R.H.J., Borst, R.D., Brekelmans, W.A.M., Vree, J.H.P.D., 1996a. Gradient enhanced damage for quasi-brittle materials. Internat. J. Numer. Methods Engrg. 39 (19), 3391–3403.

Peerlings, R.H.J., Borst, R.D., Brekelmans, W.A.M., Vree, J.H.P.D., 1996b. Some observations on localisation in non-local and gradient damage models. Eur. J. Mech. A Solids 15 (6), 937–953.

Polizzotto, C., Borino, G., Fuschi, P., 1998. A thermodynamically consistent formulation of nonlocal and gradient plasticity. Mech. Res. Commun. 25 (1), 75–82.

Pollack, J., Jean, P.F., 2012. Wave energy converter. Google Patents. US Patent 8, 120, 195.

Rawat, A., Piska, R., Rajagopal, A., Hossain, M., 2021. Nonlocal plasticity-based damage modeling in quasi-brittle materials using an isogeometric approach. Eng. Comput. 38, 2604–2630, URL https://doi.org/10.1108/EC-12-2019-0562.

Renzi, E., Michele, S., Zheng, S., Jin, S., Greaves, D., 2021. Niche applications and flexible devices for wave energy conversion: A review. Energies 14 (20), http://dx.doi.org/10.3390/en14206537, URL https://www.mdpi.com/1996-1073/14/20/6537.

Righi, M., Moretti, G., Forehand, D., Agostini, L., Vertechy, R., Fontana, M., 2021. A broadbanded pressure differential wave energy converter based on dielectric elastomer generators. Nonlinear Dynam. 105 (4), 2861–2876.

Ryan, G.L., Ryan, S.K., 2017. Wave energy conversion. Google Patents. US Patent 9, 797, 367.

Selby, J.C., Shannon, M.A., 2009. Inflation of a circular elastomeric membrane into a horizontally semi-infinite liquid reservoir of finite vertical depth: Quasi-static deformation model. Internat. J. Engrg. Sci. 47 (5), 700–717. http://dx.doi.org/10.1016/j.ijengsci.2009.01.008, URL https://www.sciencedirect.com/science/article/pii/S002072250900010X.

Shittu, A.A., Mehmanparast, A., Hart, P., Kolios, A., 2021. Comparative study between SN and fracture mechanics approach on reliability assessment of offshore wind turbine jacket foundations. Reliab. Eng. Syst. Saf. 215, 107838.

Steinmann, P., 1999. Formulation and computation of geometrically non-linear gradient damage. Internat. J. Numer. Methods Engrg. 46 (5), 757–779. http://dx.doi.org/10.1002/(SICI)1097-0207(19991020)46:5<757::AID-NME731>3.0.CO;2-N.

Steinmann, P., Hossain, M., Possart, G., 2012. Hyperelastic models for rubber-like materials: consistent tangent operators and suitability for Treloar's data. Arch. Appl. Mech. 82 (9), 1183–1217. http://dx.doi.org/10.1007/s00419-012-0610-z.

Umesh, B., Rajagopal, A., 2019. Higher order continuous approximation for the assessment of nonlocal-gradient based damage model. Mech. Adv. Mater. Struct. 26 (20), 1671–1682. http://dx.doi.org/10.1080/15376494.2018.1440038.

Verron, E., Marckmann, G., Peseux, B., 2001. Dynamic inflation of non-linear elastic and viscoelastic rubber-like membranes. Internat. J. Numer. Methods Engrg. 50 (5), 1233–1251. http://dx.doi.org/10.1002/1097-0207(20010220)50:5<1233::AID-NME77>3.0.CO;2-W, arXiv:https://onlinelibrary.wiley.com/doi/pdf/10.1002/1097-0207%2820010220%2950%3A5%3C1233%3A%3AID-NME77%3E3.0.CO%3B2-W. URL https://onlinelibrary.wiley.com/doi/abs/10.1002/1097-0207%2820010220%2950%3A5%3C1233%3A%3AID-NME77%3E3.0.CO%3B2-W.

Waffenschmidt, T., Polindara, C., Menzel, A., Blanco, S., 2014. A gradient-enhanced large-deformation continuum damage model for fibre-reinforced materials. Comput. Methods Appl. Mech. Engrg. 268, 801–842. http://dx.doi.org/10.1016/j.cma.2013.10.013, URL https://www.sciencedirect.com/science/article/pii/S004578251300265X.

Yemm, R., Pizer, D., Retzler, C., Henderson, R., 2012. Pelamis: experience from concept to connection. Phil. Trans. R. Soc. A 370 (1959), 365–380. http://dx.doi.org/10.1098/rsta.2011.0312, arXiv:https://royalsocietypublishing.org/doi/pdf/10.1098/rsta.2011.0312. URL https://royalsocietypublishing.org/doi/abs/10.1098/rsta.2011.0312.

Zheng, S., Phillips, J.W., Hann, M., Greaves, D., 2023. Mathematical modelling of a floating clam-type wave energy converter. Renew. Energy 210, 280–294. http://dx.doi.org/10.1016/j.renene.2023.04.040, URL https://www.sciencedirect.com/science/article/pii/S0960148123004901.

Zurkinden, A.S., Lambertsen, S.H., Damkilde, L., Gao, Z., Moan, T., 2013. Fatigue analysis of a wave energy converter taking into account different control strategies. In: International Conference on Offshore Mechanics and Arctic Engineering. Vol. 55423. American Society of Mechanical Engineers, V008T09A057.